

SEARCH FOR COSMIC-RAY-INDUCED GAMMA-RAY EMISSION IN GALAXY CLUSTERS

M. ACKERMANN¹, M. AJELLO², A. ALBERT³, A. ALLAFORT⁴, W. B. ATWOOD⁵, L. BALDINI⁶, J. BALLE⁷, G. BARBIELLINI^{8,9},
D. BASTIERI^{10,11}, K. BECHTOL⁴, R. BELLAZZINI¹², E. D. BLOOM⁴, E. BONAMENTE^{13,14}, E. BOTTACINI⁴, T. J. BRANDT¹⁵,
J. BREGEON¹², M. BRIGIDA^{16,17}, P. BRUEL¹⁸, R. BUEHLER¹, S. BUSON^{10,11}, G. A. CALIANDRO¹⁹, R. A. CAMERON⁴,
P. A. CARAVEO²⁰, E. CAVAZZUTI²¹, R. C. G. CHAVES⁷, J. CHIANG⁴, G. CHIARO¹¹, S. CIPRINI^{21,22}, R. CLAUS⁴, J. COHEN-TANUGI²³,
J. CONRAD^{24,25,26,57}, F. D'AMMANDO²⁷, A. DE ANGELIS²⁸, F. DE PALMA^{16,17}, C. D. DERMER²⁹, S. W. DIGEL⁴, P. S. DRELL⁴,
A. DRLICA-WAGNER⁴, C. FAVUZZI^{16,17}, A. FRANCKOWIAK⁴, S. FUNK⁴, P. FUSCO^{16,17}, F. GARGANO¹⁷, D. GASPARRINI^{21,22},
S. GERMANI^{13,14}, N. GIGLIETTO^{16,17}, F. GIORDANO^{16,17}, M. GIROLETTI²⁷, G. GODFREY⁴, G. A. GOMEZ-VARGAS^{30,31,32},
I. A. GRENIER⁷, S. GUIRIEC^{15,58}, M. GUSTAFSSON³³, D. HADASCH¹⁹, M. HAYASHIDA^{4,34}, J. HEWITT¹⁵, R. E. HUGHES³,
T. E. JELTEMA⁵, G. JÓHANNESSEN³⁵, A. S. JOHNSON⁴, T. KAMAE⁴, J. KATAOKA³⁶, J. KNÖDLSER^{37,38}, M. KUSS¹², J. LANDE⁴,
S. LARSSON^{24,25,39}, L. LATRONICO⁴⁰, M. LENA GARDE^{24,25}, F. LONGO^{8,9}, F. LOPARCO^{16,17}, M. N. LOVELLETTE²⁹, P. LUBRANO^{13,14},
M. MAYER¹, M. N. MAZZIOTTA¹⁷, J. E. MCENERY^{15,41}, P. F. MICHELSON⁴, W. MITTHUMSIRI⁴, T. MIZUNO⁴², M. E. MONZANI⁴,
A. MORSELLI³⁰, I. V. MOSKALENKO⁴, S. MURGIA⁴, R. NEMMEN¹⁵, E. NUSS²³, T. OHSUGI⁴², M. ORIENTI²⁷, E. ORLANDO⁴,
J. F. ORMES⁴³, J. S. PERKINS¹⁵, M. PESCE-ROLLINS¹², F. PIRON²³, G. PIVATO¹¹, S. RAINÒ^{16,17}, R. RANDO^{10,11}, M. RAZZANO^{5,12},
S. RAZZAQUE⁴⁴, A. REIMER^{4,45}, O. REIMER^{4,45}, J. RUAN⁴⁶, M. SÁNCHEZ-CONDE⁴, A. SCHULZ¹, C. SGRÒ¹², E. J. SISKIND⁴⁷,
G. SPANDRE¹², P. SPINELLI^{16,17}, E. STORM⁵, A. W. STRONG⁴⁸, D. J. SUSON⁴⁹, H. TAKAHASHI⁵⁰, J. G. THAYER⁴, J. B. THAYER⁴,
D. J. THOMPSON¹⁵, L. TIBALDO⁴, M. TINIVELLA¹², D. F. TORRES^{19,51}, E. TROJA^{15,41}, Y. UCHIYAMA⁵², T. L. USHER⁴,
J. VANDENBROUCKE⁴, G. VIANELLO^{4,53}, V. VITALE^{30,54}, B. L. WINER³, K. S. WOOD²⁹, AND S. ZIMMER^{24,25}

(THE FERMI-LAT COLLABORATION)

AND

A. PINZKE^{55,59}, AND C. PFROMMER⁵⁶¹ Deutsches Elektronen Synchrotron DESY, D-15738 Zeuthen, Germany² Space Sciences Laboratory, 7 Gauss Way, University of California, Berkeley, CA 94720-7450, USA³ Department of Physics, Center for Cosmology and Astro-Particle Physics, The Ohio State University, Columbus, OH 43210, USA⁴ W. W. Hansen Experimental Physics Laboratory, Kavli Institute for Particle Astrophysics and Cosmology, Department of Physics and SLAC National Accelerator Laboratory, Stanford University, Stanford, CA 94305, USA; olr@slac.stanford.edu⁵ Santa Cruz Institute for Particle Physics, Department of Physics and Department of Astronomy and Astrophysics, University of California at Santa Cruz, Santa Cruz, CA 95064, USA⁶ Università di Pisa and Istituto Nazionale di Fisica Nucleare, Sezione di Pisa I-56127 Pisa, Italy⁷ Laboratoire AIM, CEA-IRFU/CNRS/Université Paris Diderot, Service d'Astrophysique, CEA Saclay, F-91191 Gif sur Yvette, France⁸ Istituto Nazionale di Fisica Nucleare, Sezione di Trieste, I-34127 Trieste, Italy⁹ Dipartimento di Fisica, Università di Trieste, I-34127 Trieste, Italy¹⁰ Istituto Nazionale di Fisica Nucleare, Sezione di Padova, I-35131 Padova, Italy¹¹ Dipartimento di Fisica e Astronomia "G. Galilei," Università di Padova, I-35131 Padova, Italy¹² Istituto Nazionale di Fisica Nucleare, Sezione di Pisa, I-56127 Pisa, Italy¹³ Istituto Nazionale di Fisica Nucleare, Sezione di Perugia, I-06123 Perugia, Italy¹⁴ Dipartimento di Fisica, Università degli Studi di Perugia, I-06123 Perugia, Italy¹⁵ NASA Goddard Space Flight Center, Greenbelt, MD 20771, USA¹⁶ Dipartimento di Fisica "M. Merlin" dell'Università e del Politecnico di Bari, I-70126 Bari, Italy¹⁷ Istituto Nazionale di Fisica Nucleare, Sezione di Bari, I-70126 Bari, Italy¹⁸ Laboratoire Leprince-Ringuet, École polytechnique, CNRS/IN2P3, F-91128 Palaiseau, France¹⁹ Institut de Ciències de l'Espai (IEEE-CSIC), Campus UAB, E-08193 Barcelona, Spain²⁰ INAF-Istituto di Astrofisica Spaziale e Fisica Cosmica, I-20133 Milano, Italy²¹ Agenzia Spaziale Italiana (ASI) Science Data Center, I-00044 Frascati (Roma), Italy²² Istituto Nazionale di Astrofisica-Osservatorio Astronomico di Roma, I-00040 Monte Porzio Catone (Roma), Italy²³ Laboratoire Univers et Particules de Montpellier, Université Montpellier 2, CNRS/IN2P3, F-34095 Montpellier, France²⁴ Department of Physics, Stockholm University, AlbaNova, SE-106 91 Stockholm, Sweden; zimmer@fysik.su.se, conrad@fysik.su.se²⁵ The Oskar Klein Centre for Cosmoparticle Physics, AlbaNova, SE-106 91 Stockholm, Sweden²⁶ The Royal Swedish Academy of Sciences, Box 50005, SE-104 05 Stockholm, Sweden²⁷ INAF Istituto di Radioastronomia, I-40129 Bologna, Italy²⁸ Dipartimento di Fisica, Università di Udine and Istituto Nazionale di Fisica Nucleare, Sezione di Trieste, Gruppo Collegato di Udine, I-33100 Udine, Italy²⁹ Space Science Division, Naval Research Laboratory, Washington, DC 20375-5352, USA³⁰ Istituto Nazionale di Fisica Nucleare, Sezione di Roma "Tor Vergata," I-00133 Roma, Italy³¹ Departamento de Física Teórica, Universidad Autónoma de Madrid, Cantoblanco, E-28049 Madrid, Spain³² Instituto de Física Teórica IFT-UAM/CSIC, Universidad Autónoma de Madrid, Cantoblanco, E-28049 Madrid, Spain³³ Service de Physique Théorique, Université Libre de Bruxelles (ULB), Bld du Triomphe, CP225, B-1050 Brussels, Belgium³⁴ Institute for Cosmic-Ray Research, University of Tokyo, 5-1-5 Kashiwanoha, Kashiwa, Chiba 277-8582, Japan³⁵ Science Institute, University of Iceland, IS-107 Reykjavik, Iceland³⁶ Research Institute for Science and Engineering, Waseda University, 3-4-1, Okubo, Shinjuku, Tokyo 169-8555, Japan³⁷ CNRS, IRAP, F-31028 Toulouse cedex 4, France³⁸ GAHEC, Université de Toulouse, UPS-OMP, IRAP, F-91191 Toulouse, France³⁹ Department of Astronomy, Stockholm University, SE-106 91 Stockholm, Sweden⁴⁰ Istituto Nazionale di Fisica Nucleare, Sezione di Torino, I-10125 Torino, Italy⁴¹ Department of Physics and Department of Astronomy, University of Maryland, College Park, MD 20742, USA⁴² Hiroshima Astrophysical Science Center, Hiroshima University, Higashi-Hiroshima, Hiroshima 739-8526, Japan⁴³ Department of Physics and Astronomy, University of Denver, Denver, CO 80208, USA⁴⁴ Department of Physics, University of Johannesburg, Auckland Park 2006, South Africa

⁴⁵ Institut für Astro- und Teilchenphysik and Institut für Theoretische Physik, Leopold-Franzens-Universität Innsbruck, A-6020 Innsbruck, Austria

⁴⁶ Department of Physics, Washington University, St. Louis, MO 63130, USA

⁴⁷ NYCB Real-Time Computing Inc., Lattigtown, NY 11560-1025, USA

⁴⁸ Max-Planck Institut für extraterrestrische Physik, D-85748 Garching, Germany

⁴⁹ Department of Chemistry and Physics, Purdue University Calumet, Hammond, IN 46323-2094, USA

⁵⁰ Department of Physical Sciences, Hiroshima University, Higashi-Hiroshima, Hiroshima 739-8526, Japan

⁵¹ Institució Catalana de Recerca i Estudis Avançats (ICREA), E-08034 Barcelona, Spain

⁵² 3-34-1 Nishi-Ikebukuro, Toshima-ku, Tokyo 171-8501, Japan

⁵³ Consorzio Interuniversitario per la Fisica Spaziale (CIFS), I-10133 Torino, Italy

⁵⁴ Dipartimento di Fisica, Università di Roma “Tor Vergata,” I-00133 Roma, Italy

⁵⁵ Department of Physics, University of California, Santa Barbara, CA 93106-9530, USA; apinzke@fysik.su.se

⁵⁶ Heidelberg Institute for Theoretical Studies, Schloss-Wolfsbrunnengasse 35, D-69118 Heidelberg, Germany; christoph.pfrommer@h-its.org

Received 2013 August 26; accepted 2014 March 20; published 2014 April 30

ABSTRACT

Current theories predict relativistic hadronic particle populations in clusters of galaxies in addition to the already observed relativistic leptons. In these scenarios hadronic interactions give rise to neutral pions which decay into γ rays that are potentially observable with the Large Area Telescope (LAT) on board the *Fermi* space telescope. We present a joint likelihood analysis searching for spatially extended γ -ray emission at the locations of 50 galaxy clusters in four years of *Fermi*-LAT data under the assumption of the universal cosmic-ray (CR) model proposed by Pinzke & Pfrommer. We find an excess at a significance of 2.7σ , which upon closer inspection, however, is correlated to *individual* excess emission toward three galaxy clusters: A400, A1367, and A3112. We discuss these cases in detail and conservatively attribute the emission to unmodeled background systems (for example, radio galaxies within the clusters). Through the combined analysis of 50 clusters, we exclude hadronic injection efficiencies in simple hadronic models above 21% and establish limits on the CR to thermal pressure ratio within the virial radius, R_{200} , to be below 1.25%–1.4% depending on the morphological classification. In addition, we derive new limits on the γ -ray flux from individual clusters in our sample.

Key words: galaxies: clusters: intracluster medium – gamma rays: galaxies: clusters

Online-only material: color figures

1. INTRODUCTION

The quest for the first detection of high-energy γ rays from galaxy clusters is still ongoing. While there have been γ -ray detections from radio galaxies in clusters such as NGC 1275 (Strong & Bignami 1983; Abdo et al. 2009; Aleksić et al. 2012b) and IC 310 (Aleksić et al. 2010a; Neronov et al. 2010) in the Perseus cluster, as well as M87 in the Virgo cluster (Sreekumar et al. 1994; Abdo et al. 2009; Aharonian et al. 2003), no cluster-wide γ -ray emission has been detected so far. Previous reports of space-based cluster observations in the GeV band include Reimer et al. 2003, Ackermann et al. 2010b, Zimmer et al. 2011, Ando & Nagai 2012, and Han et al. 2012. Ground-based observations in the energy band $\gtrsim 100$ GeV were reported for Perseus and A2029 by Perkins et al. (2006), for A496 and A85 by Aharonian et al. (2009b), for Coma by Aharonian et al. (2009a); Arlen et al. (2012), for A3667 and A4038 by Kiuchi et al. (2009), for Perseus by Aleksić et al. (2010a, 2012a), and for Fornax by Abramowski et al. (2012). Nevertheless, current space-based γ -ray detectors such as the Large Area Telescope (LAT) on board the *Fermi* satellite (Atwood et al. 2009) may be able to detect γ rays from galaxy clusters during its lifetime.

The discovery and characterization of cosmic-ray-induced (CR-induced) γ rays from clusters could not only serve as a crucial discriminator between different models for the observed cluster-wide radio emission (Pfrommer & Enßlin 2004a; Brunetti et al. 2012) but could also be a signpost of the physical

heating processes underlying feedback by active galactic nuclei (AGNs) that has been proposed to solve the “cluster cooling flow problem” (Loewenstein et al. 1991; Guo & Oh 2008; Enßlin et al. 2011; Fujita & Ohira 2012; Wiener et al. 2013; Pfrommer 2013). Moreover, any observed γ -ray emission from clusters necessarily requires a detailed understanding of the astrophysical γ -ray contribution before putting forward constraints on more exotic scenarios such as annihilation or decay signals from dark matter (DM; Ackermann et al. 2010a; Dugger et al. 2010; Pinzke et al. 2011; Huang et al. 2012).

The intracluster medium (ICM) consists of a hot (1–10 keV) plasma, which has primarily been heated through collisionless shocks that form as a result of the hierarchical build-up of galaxy clusters (e.g., Ryu et al. 2003; Pfrommer et al. 2006; Skillman et al. 2008; Vazza et al. 2009). These structure formation shocks and the turbulent motions of the gas in combination with intracluster magnetic fields provide the necessary conditions for efficient particle acceleration (e.g., Colafrancesco & Blasi 1998; Ryu et al. 2003). Recent radio observations prove the existence of relativistic electrons and magnetic fields in clusters. Some cool core (CC) clusters host radio mini halos in their centers (Enßlin et al. 2011). Additionally, a subsample of merging non-cool core (NCC) clusters show radio relics at their periphery (Kempner et al. 2004) and/or giant radio halos that often extend out to Mpc scales. While giant radio halos have been observed in more than 50 clusters (see, e.g., Ferrari et al. 2008, for a review), their precise origin is still not understood. There are two competing theories to explain these radio halos.

In *hadronic models*, CR ions and protons (p) are accelerated in structure formation shocks, jets of radio galaxies, and supernovae-driven galactic winds (see, e.g., Völk et al. 1996; Enßlin et al. 1997; Berezhinsky et al. 1997; Pfrommer & Enßlin

⁵⁷ Royal Swedish Academy of Sciences Research Fellow, funded by a grant from the K. A. Wallenberg Foundation.

⁵⁸ NASA Postdoctoral Program Fellow, USA.

⁵⁹ Current address: The Oskar Klein Centre for Cosmoparticle Physics, AlbaNova, SE-106 91 Stockholm, Sweden.

2004a), and significant populations of CR protons can accumulate due to their long cooling time in the ICM (Völk et al. 1996). Inelastic collisions of CR ions with thermal protons of the ICM produce both neutral and charged pions, which decay almost instantly into γ rays and electrons/positrons, respectively. This process could in principle account for the radio-emitting leptons, while requiring only a modest CR-to-thermal pressure ratio of (at most) a few percent (Dennison 1980; Vestrand 1982; Blasi & Colafrancesco 1999; Dolag & Enßlin 2000; Miniati et al. 2001a, 2001b; Miniati 2003; Pfrommer & Enßlin 2003, 2004a, 2004b; Blasi et al. 2007; Pfrommer et al. 2008; Pfrommer 2008; Kushnir et al. 2009; Donnert et al. 2010a, 2010b; Keshet & Loeb 2010; Keshet 2010; Enßlin et al. 2011). The non-detection of γ -ray emission from individual radio halo clusters places strong limits on intracluster magnetic fields within the hadronic model (Pfrommer & Enßlin 2004b; Jeltama & Profumo 2011; Arlen et al. 2012; Brunetti et al. 2012; Aleksić et al. 2012a). The secondary leptons also experience Compton upscattering with the background radiation fields to γ -ray energies, but this expected emission is always subdominant compared to the γ rays produced by decaying neutral pions (Miniati 2003; Pfrommer et al. 2008; Pinzke & Pfrommer 2010).

The *re-acceleration models* assume the existence of a long-lived pool of mildly relativistic electrons, that were accelerated in the past by structure formation shocks, galactic winds, and AGNs, or coincide with secondary electrons that are injected in the aforementioned hadronic CR p - p interactions. Those CR electrons scatter with plasma waves that are excited by ICM turbulence, e.g., after a cluster merger. These particle-wave interactions may accelerate the particles through the second order Fermi process to sufficiently high energies to explain the observed radio emission (Schlickeiser et al. 1987; Brunetti et al. 2001; Petrosian 2001; Brunetti et al. 2004; Brunetti & Blasi 2005; Brunetti & Lazarian 2007, 2011; Brunetti et al. 2009; Donnert et al. 2013).

Assuming that the same physical processes that produce γ rays are present in each galaxy cluster, independent of mass, age, and other characteristics, we employ a joint likelihood analysis to search for these γ rays. The resulting universal scaling factor A_γ can be used to derive limits on the hadronic acceleration efficiency at structure formation shocks and the volume-averaged CR-to-thermal pressure $\langle X_{\text{CR}} \rangle$. While the joint likelihood method can be applied to study any emission governed by a universal physical process, in this paper, we focus on the search for γ rays from CR-induced pion decay and defer more exotic scenarios such as γ rays from DM annihilation and decay to future studies.

The outline of this paper is as follows. We discuss our cluster selection in Section 2 and address the *Fermi*-LAT observations and data analysis in Section 3. Our cluster emission models are described in Section 4. We present and discuss our results in Section 5. Finally, we present a survey of possible systematics in Section 6, and we conclude in Section 7. Throughout the paper, we assume a cosmology with $\Omega_m = 0.3$, $\Omega_\Lambda = 0.7$, and $h = 0.7$.

2. CLUSTER SELECTION

Assuming a correlation between γ -ray and X-ray luminosity in galaxy clusters (Colafrancesco & Blasi 1998; Pfrommer & Enßlin 2004a), we use the extended Highest X-ray Flux Galaxy Cluster Sample (HIFLUGCS; Reiprich & Böhringer 2002; Chen et al. 2007), containing the 106 nearby brightest X-ray clusters

from the *ROSAT* all-sky survey, as a suitable list of sources when constructing our analysis sample.

Given that our statistical approach assumes independent sources, we remove clusters where the angular separation between cluster centers is less than any of the respective virial radii enlarged by 1° .⁶⁰ This cut is motivated by Monte Carlo (MC) studies (see Appendix A.1 for details), showing that for an energy threshold of 500 MeV, the bias on the likelihood ratio test statistic due to overlaps is minimal under the condition above. However, in the case that the expected γ -ray flux from a single HIFLUGCS cluster within such an ensemble of overlapping clusters is responsible for more than 90% of the total expected emission, as calculated using the approach in Pinzke et al. (2011), we neglect the other clusters in the ensemble and attribute all photons to the cluster with the largest expected flux.

The aforementioned virial radius, R_{200} , of the cluster is the radius containing the virial mass, M_{200} , which in turn is derived from the M_{500} mass reported by Chen et al. (2007).⁶¹ We solve for M_{200} using $M_{200} = M_{500} \times 200/500 \times [c_{200}(M_{200})/c_{500}(M_{200})]^3$ (Voit 2005), where the halo-mass-dependent concentration parameter c is derived from a power-law fit to a sample of observed galaxy cluster concentration and masses (Comerford & Natarajan 2007).

The extended HIFLUGCS catalog contains clusters up to redshifts of 0.18, with the majority located at $z < 0.1$. For simplicity, we do not apply a redshift correction to the spectrum, and we decided to exclude all clusters above $z = 0.1$, as their inclusion without applying a correction would amount to incorrect modeling of the spectrum. These clusters contribute less than 1% to the total expected γ -ray flux including all clusters in the HIFLUGCS catalog, as derived in Pinzke et al. (2011), making this a suitable approach. In addition, we exclude clusters that lie in a box defined by $|b| \leq 50^\circ$ and $|l| \leq 20^\circ$, as this region contains emission from the Galactic plane and the *Fermi* bubbles (Su et al. 2010), the models for which have relatively large systematic uncertainties. The Virgo cluster, which has a virial radius of $\sim 8^\circ$ on the sky (Fouqué et al. 2001) and clusters that fall into this region, such as M49, is excluded from the analysis.

The Galactic plane presents a substantial challenge due to a large number of potentially unresolved point sources and uncertainties in modeling the diffuse foregrounds. We conservatively define the plane region to be $|b| \leq 20^\circ$ and remove clusters from our sample that lie within this region, such as the Centaurus cluster. There are nine Abell clusters present in the HIFLUGCS catalog that are located within a radius of 7° from the center of the Centaurus cluster which overlap with one another. In order to avoid highly crowded analysis regions, we exclude the entire region.

The remaining clusters are considered separately according to their classification as either CC, NCC, or unclassified. For this purpose, we use the classification presented in Hudson et al. (2010) or follow recommendations by Cavagnolo et al. (2009). Among other quantities, we classify clusters that have central entropy values $K_0 \leq 30 \text{ keV cm}^2$ as CC and otherwise as NCC. When there is no supporting X-ray data available, we leave these clusters unclassified.

The 50 galaxy clusters we consider in this analysis are listed in Table 1 along with characteristic cluster quantities

⁶⁰ All cluster positions, which were taken from the NASA Extragalactic Database (<http://ned.ipac.caltech.edu/>), are based on observations in the optical waveband.

⁶¹ We define the virial radius of a cluster as the radius at which the mean interior density equals 200 times the *critical density* of the universe.

Table 1
Cluster Sample Considered for the Analysis

| Name | R.A. ($^{\circ}$) | Decl. ($^{\circ}$) | z | R_{200} (Mpc) | M_{200} ($\times 10^{15}$) | Ext. ($^{\circ}$) | $F_{\gamma, \text{exp}}^{\text{CR}}(E > 500 \text{ MeV})$ ($10^{-10} \text{ ph cm}^{-2} \text{ s}^{-1}$) | $\langle X_{\text{CR}} \rangle_{R_{\text{HL}}}$ ($\times 10^{-1}$) | $\langle X_{\text{CR}} \rangle_{R_{200}}$ ($\times 10^{-1}$) | Morph. |
|---------------|------------------------|-------------------------|------|--------------------|-----------------------------------|------------------------|---|---|---|------------------|
| 2A0335 | 54.65 | 9.97 | 0.04 | 1.31 | 0.26 | 1.06 | 2.84 | 0.32 | 0.14 | CC |
| A0085 | 10.41 | -9.34 | 0.06 | 1.89 | 0.78 | 1.00 | 2.93 | 0.24 | 0.10 | CC |
| A0119 | 14.09 | -1.26 | 0.04 | 1.96 | 0.86 | 1.27 | 1.42 | 0.24 | 0.14 | NCC |
| A0133 | 15.66 | -21.96 | 0.06 | 1.52 | 0.41 | 0.78 | 0.72 | 0.28 | 0.13 | CC |
| A0262 | 28.21 | 36.15 | 0.02 | 0.91 | 0.09 | 1.54 | 1.21 | 0.41 | 0.30 | CC |
| A0400 | 44.41 | 6.03 | 0.02 | 1.02 | 0.12 | 1.17 | 0.44 | 0.38 | 0.28 | NCC |
| A0478 | 63.34 | 10.48 | 0.09 | 1.95 | 0.86 | 0.67 | 2.45 | 0.24 | 0.09 | CC |
| A0496 | 68.41 | -13.25 | 0.03 | 1.58 | 0.46 | 1.36 | 2.83 | 0.28 | 0.12 | CC |
| A0548e | 87.16 | -25.47 | 0.04 | 1.06 | 0.14 | 0.76 | 0.25 | 0.37 | 0.26 | ? |
| A0576 | 110.35 | 55.74 | 0.04 | 1.56 | 0.44 | 1.14 | 0.63 | 0.28 | 0.16 | NCC ^a |
| A0754 | 137.21 | -9.64 | 0.05 | 2.27 | 1.35 | 1.22 | 1.69 | 0.21 | 0.08 | NCC |
| A1060 (Hydra) | 159.21 | -27.53 | 0.01 | 1.26 | 0.23 | 2.77 | 2.28 | 0.33 | 0.18 | CC |
| A1367 (Leo) | 176.12 | 19.84 | 0.02 | 1.83 | 0.71 | 2.33 | 1.92 | 0.25 | 0.13 | NCC |
| A1644 | 194.31 | -17.35 | 0.05 | 1.83 | 0.70 | 1.11 | 1.30 | 0.25 | 0.14 | CC |
| A1795 | 207.25 | 26.59 | 0.06 | 2.02 | 0.95 | 0.95 | 3.01 | 0.23 | 0.11 | CC |
| A2065 | 230.68 | 27.72 | 0.07 | 2.11 | 1.09 | 0.86 | 0.92 | 0.21 | 0.08 | CC |
| A2142 | 239.57 | 27.22 | 0.09 | 2.30 | 1.40 | 0.77 | 3.45 | 0.29 | 0.14 | CC |
| A2199 | 247.16 | 39.55 | 0.03 | 1.52 | 0.40 | 1.42 | 3.00 | 0.27 | 0.13 | CC |
| A2244 | 255.68 | 34.05 | 0.10 | 1.66 | 0.52 | 0.52 | 0.76 | 0.25 | 0.14 | CC |
| A2255 | 258.13 | 64.09 | 0.08 | 1.87 | 0.76 | 0.69 | 0.85 | 0.22 | 0.11 | NCC ^b |
| A2256 | 255.93 | 78.72 | 0.06 | 2.17 | 1.18 | 1.09 | 2.55 | 0.31 | 0.17 | NCC ^b |
| A2589 | 351.00 | 16.82 | 0.04 | 1.38 | 0.30 | 0.95 | 0.68 | 0.30 | 0.13 | CC |
| A2597 | 351.33 | -12.11 | 0.09 | 1.45 | 0.35 | 0.51 | 0.76 | 0.28 | 0.17 | CC |
| A2634 | 354.58 | 27.03 | 0.03 | 1.55 | 0.43 | 1.39 | 0.62 | 0.26 | 0.13 | CC |
| A2657 | 356.21 | 9.14 | 0.04 | 1.71 | 0.58 | 1.21 | 0.83 | 0.28 | 0.15 | CC |
| A2734 | 2.83 | -28.87 | 0.06 | 1.58 | 0.46 | 0.74 | 0.44 | 0.26 | 0.12 | NCC |
| A2877 | 17.46 | -45.90 | 0.03 | 1.78 | 0.65 | 2.03 | 0.51 | 0.28 | 0.12 | NCC ^b |
| A3112 | 49.47 | -44.24 | 0.08 | 1.53 | 0.41 | 0.60 | 1.11 | 0.27 | 0.14 | CC |
| A3158 | 55.67 | -53.63 | 0.06 | 1.68 | 0.55 | 0.82 | 1.20 | 0.20 | 0.09 | NCC |
| A3266 | 67.80 | -61.41 | 0.06 | 2.54 | 1.89 | 1.26 | 3.13 | 0.26 | 0.15 | CC |
| A3376 | 90.18 | -40.05 | 0.05 | 1.78 | 0.65 | 1.12 | 0.69 | 0.27 | 0.17 | NCC |
| A3822 | 328.53 | -57.85 | 0.08 | 1.57 | 0.45 | 0.61 | 0.45 | 0.28 | 0.17 | NCC ^a |
| A3827 | 330.45 | -59.95 | 0.10 | 2.36 | 1.52 | 0.73 | 0.98 | 0.21 | 0.09 | NCC ^a |
| A3921 | 342.41 | -64.39 | 0.09 | 1.77 | 0.63 | 0.58 | 0.47 | 0.26 | 0.13 | NCC ^a |
| A4038 | 356.90 | -28.13 | 0.03 | 1.28 | 0.24 | 1.20 | 1.34 | 0.32 | 0.17 | CC |
| A4059 | 359.17 | -34.67 | 0.05 | 1.54 | 0.42 | 0.93 | 0.97 | 0.28 | 0.13 | CC |
| COMA | 194.95 | 27.98 | 0.02 | 2.02 | 0.96 | 2.46 | 11.40 | 0.23 | 0.12 | NCC |
| EXO0422 | 62.93 | -29.81 | 0.04 | 1.30 | 0.25 | 0.93 | 0.72 | 0.32 | 0.17 | CC |
| FORNAX | 54.63 | -35.46 | 0.01 | 1.01 | 0.12 | 5.98 | 0.84 | 0.38 | 0.25 | CC |
| HCG94 | 349.32 | 18.72 | 0.04 | 1.22 | 0.21 | 0.83 | 0.38 | 0.33 | 0.21 | ? |
| HYDRA-A | 139.52 | -12.10 | 0.06 | 1.50 | 0.38 | 0.79 | 1.67 | 0.29 | 0.12 | CC |
| II Zw 54 | 55.32 | 15.40 | 0.03 | 1.45 | 0.35 | 1.41 | 0.45 | 0.30 | 0.16 | CC |
| II Zw 108 | 318.48 | 2.57 | 0.05 | 1.47 | 0.36 | 0.86 | 0.40 | 0.29 | 0.19 | ? |
| NGC 1550 | 64.91 | 2.41 | 0.01 | 0.81 | 0.06 | 1.80 | 0.67 | 0.45 | 0.33 | CC |
| NGC 5044 | 198.85 | -16.39 | 0.01 | 0.73 | 0.04 | 2.14 | 0.61 | 0.50 | 0.42 | CC |
| RXJ2344 | 356.07 | -4.37 | 0.08 | 1.95 | 0.86 | 0.74 | 0.57 | 0.24 | 0.11 | CC |
| S405 | 57.89 | -82.22 | 0.06 | 1.56 | 0.44 | 0.74 | 0.40 | 0.28 | 0.18 | CC ^a |
| S540 | 85.03 | -40.84 | 0.04 | 1.27 | 0.24 | 1.00 | 0.35 | 0.32 | 0.18 | NCC |
| UGC03957 | 115.24 | 55.43 | 0.03 | 1.39 | 0.31 | 1.15 | 0.50 | 0.30 | 0.15 | ? |
| ZwCl1742 | 266.06 | 32.98 | 0.08 | 2.04 | 0.98 | 0.80 | 1.17 | 0.23 | 0.10 | CC |

Notes. The sample we used to carry out our analysis. The locations are taken from the NED database. The columns from left to right read: cluster name according to Reiprich & Böhringer (2002); right ascension (J2000); declination (J2000); redshift, R_{200} ; M_{200} in units of M_{\odot}/H_{70} ; extension ($2 \times \theta_{200}$, where θ_{200} refers to the angular virial radius as described in footnote 62); expected γ -ray flux above 500 MeV; CR-to-thermal pressure ratio within R_{200} and the half-light radius, R_{HL} (see Section 4.1 and footnote 66 for details); and morphological classification. We denote unclassified clusters with a question mark. We note that columns 8–10 are based on the predictions in Pinzke et al. (2011) and assume $A_{\gamma} = 1$. Redshifts are from Chen et al. (2007) and references therein. M_{200} and R_{200} are calculated from R_{500} and M_{500} in the aforementioned reference. Unless specified otherwise, all classifications are from Hudson et al. (2010).

^a Values and classifications are from Sivanandam et al. (2009).

^b Values and classifications are taken from the ACCEPT database (Cavagnolo et al. 2009).

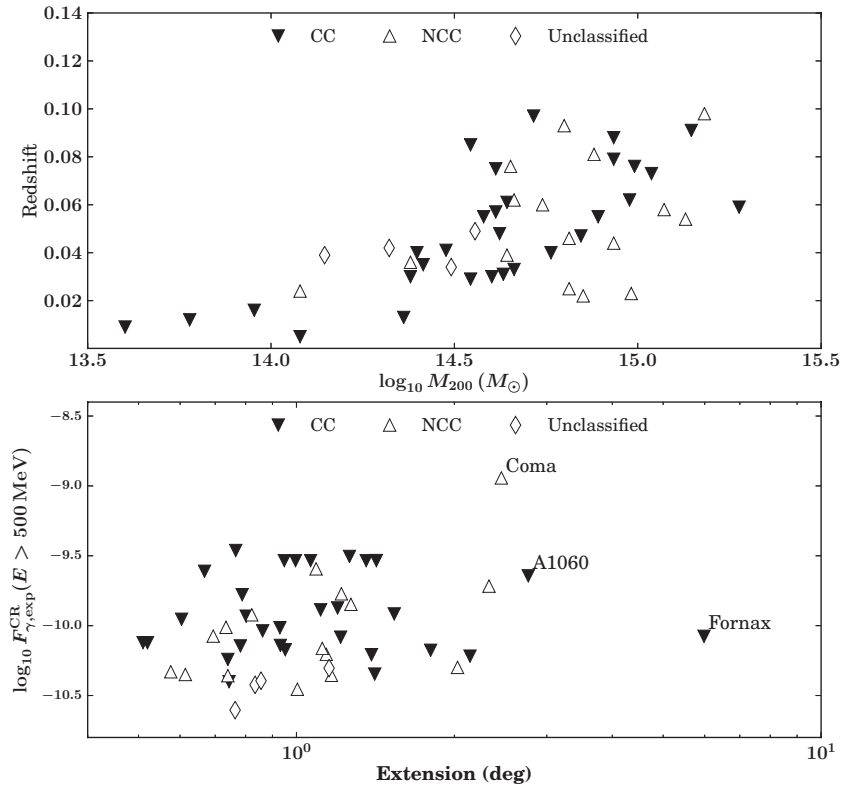


Figure 1. Summary of cluster quantities in our analysis. In the upper panel, we show redshift vs. M_{200} and in the lower panel the predicted γ -ray flux above 500 MeV taken from Pinzke et al. (2011), $F_{\gamma,\text{exp}}^{\text{CR}}(E > 500 \text{ MeV})$ vs. its extension ($= 2 \times \theta_{200}$) in degrees. Most of the selected clusters in the sample have extensions of $\sim 1^\circ$.

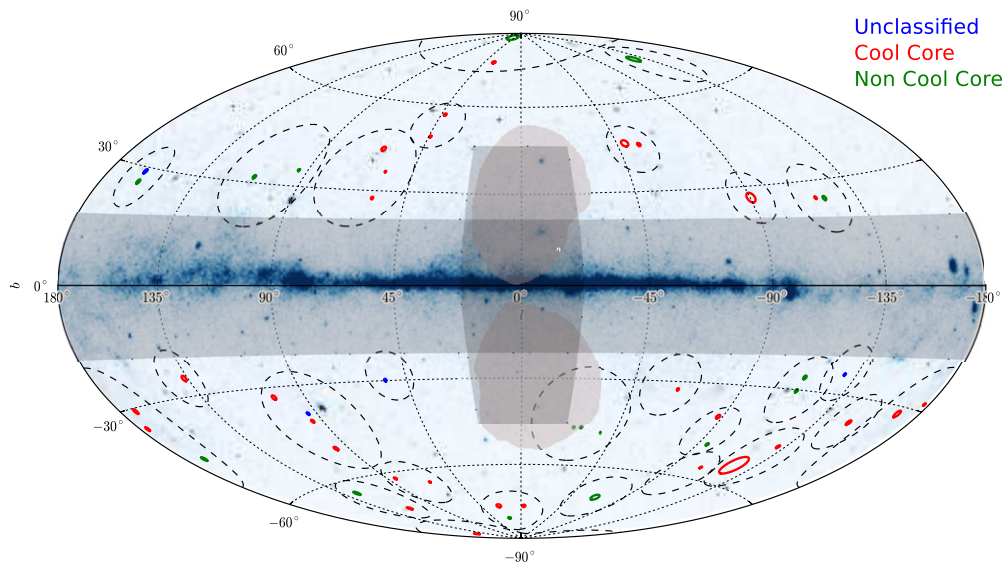


Figure 2. Hammer–Aitoff projection of the sky as seen by the LAT after four years of exposure. Shown is a counts map generated for CLEAN class events in the energy range from 500 MeV to 200 GeV using the same set of quality cuts as described in Section 3. The dashed circles correspond to the analysis regions considered for this analysis. The solid circles represent the clusters used in this analysis and their extension as characterized by their virial radii. In red we show CC, in green NCC, and in blue unclassified clusters. We shade the region which is described by the *Fermi* bubbles in Su et al. (2010) while schematically overlaying our geometric cuts for masking the Galactic plane ($|b| \leq 20^\circ$) and the Galactic bubbles ($|b| \leq 50^\circ$ and $|l| \leq 20^\circ$). The latter has been designed to mask out the majority of the emission that can be attributed to the lobes. When comparing our mask with the geometric description by Su et al. (2010), we found that two clusters are contained inside the bubbles. We checked that the region containing these two clusters is modeled well and hence keep the clusters in our analysis.

(A color version of this figure is available in the online journal.)

(see Figure 1) and their classification. We show their location and radial extension on the sky in Figure 2.⁶²

⁶² The extension we use is twice the angle subtended by the angular virial radius, θ_{200} , which is given by $\theta_{200} = \arctan(R_{200}/D_a) \times 180^\circ/\pi$, where D_a is the angular diameter distance from the Earth to the center of the cluster.

3. *Fermi*-LAT OBSERVATIONS AND DATA ANALYSIS

Fermi-LAT is the main instrument on board the *Fermi* Gamma-ray Space Telescope. Since its launch in 2008, the LAT has surveyed the γ -ray sky in the energy range from 20 MeV to >300 GeV with unprecedented sensitivity. For more details

about the LAT, the reader is referred to Atwood et al. (2009) and to Ackermann et al. (2012a) for the on-orbit LAT performance. We carry out a binned likelihood analysis of 48 months of *Fermi*-LAT data (2008 August 4–2012 August 4), which has been reprocessed to account for the time-dependent calorimeter response (Bregeon et al. 2013), and we refer to this data as P7REP. We select events corresponding to the CLEAN class, which consists of the events that have the highest probability of being γ rays, and we use the P7REP_V15 instrument response functions (IRFs) provided in the software package *Fermi Science Tools* v9r32p5.⁶³ We apply standard quality cuts to our data using `gtmktime` and require `DATA_QUAL==1 && LAT_CONFIG==1`, which refers to the configuration during nominal science operation. We require the magnitude of the rocking angle of the LAT to be $\leq 52^\circ$ and reject events above a zenith angle of 100° to greatly reduce contamination by Earth limb emission. We use `gtbin` to bin the data in 0.1° spatial bins.⁶⁴ The spectra are binned in 18 logarithmically spaced bins from 500 MeV to 200 GeV. Above 200 GeV, the number of expected events given the models and the number of detected events are both sufficiently low that the models are not well constrained, so we omit this energy range from our analysis.

3.1. Joint Likelihood

The joint likelihood is a source stacking technique, which has been previously applied with LAT data in the search for DM (Ackermann et al. 2011) and to study the extragalactic background light (Ackermann et al. 2012b). In brief, if the goal is to constrain or estimate a single or a set of parameters common to a source class, then backgrounds and individual properties of each source can be modeled individually and treated as nuisance parameters in source-specific likelihoods. The source-specific likelihoods can then be multiplied to yield a joint likelihood function that is used for inference on the common parameter of interest. The joint likelihood function for our case can be written as

$$\mathcal{L}(A_\gamma|\mathcal{D}) = \prod_i \mathcal{L}_i(A_\gamma, b_i|\mathcal{D}_i), \quad (1)$$

where A_γ is a (dimensionless) universal scale factor which serves as the parameter of interest and \mathcal{D} refers to the photon data for all regions-of-interest (ROIs). The physical interpretation of the universal scale factor in terms of CR-induced γ -ray emission is discussed further in Section 4.1. The b_i parameters correspond to the parameters describing the background components in the individual ROIs and are treated as nuisance parameters in the likelihood evaluation. The b_i s include the normalizations of the isotropic and Galactic diffuse components. We denote the photon data for each ROI as \mathcal{D}_i . The index i runs over the ROIs in the sample. Having constructed the likelihood function, we use the profile likelihood method (e.g., Rolke et al. 2005) to obtain the best-fit values and confidence intervals for the parameter of interest, A_γ . We constrain our parameter of interest and nuisance parameters to be positive. The joint likelihood function is implemented in the *Fermi Science Tools* using the `Composite2` package, and profiling over the likelihood function is achieved by means of MINOS, which is part of the

MINUIT package (James & Roos 1975). The 90% confidence interval, $[A_\gamma^{\text{LL}}, A_\gamma^{\text{UL}}]$ is defined as the values of A_γ where the log-likelihood has changed by 2.71/2 with respect to its value at the maximum, $-2\Delta \log \mathcal{L} = 2.71$ (Bartlett 1953; Rolke et al. 2005). These intervals can be reinterpreted as upper limits at the 95% confidence level (C.L.), if the parameter is unconstrained in the fit, which we do if the lower limit ≤ 0 .

For quantifying the significance of a potential excess, we employ the common likelihood ratio approach (Neyman & Pearson 1928):

$$\text{TS} = -2 \log \left(\frac{\mathcal{L}(A_\gamma = 0, \hat{b})}{\mathcal{L}(\hat{A}_\gamma, \hat{b})} \right), \quad (2)$$

where $\mathcal{L}(A_\gamma = 0, \hat{b})$ is the null hypothesis, i.e., it represents the likelihood evaluated at the best-fit \hat{b} under the background-only hypothesis (Section 5.1) and $\mathcal{L}(\hat{A}_\gamma, \hat{b})$ is the likelihood evaluated at the best-fit value of \hat{A}_γ, \hat{b} , when including our candidate γ -ray (cluster) source.

As we constrain the signal fit parameter $A_\gamma \geq 0$, the null distribution of the test statistic, TS, is given by $(1/2)\delta + (1/2)\chi^2$ for one degree of freedom (Chernoff 1952), which we verified by MC simulations. For details, the reader is referred to Appendix A. While these simulations agree well with the expectations from Chernoff's theorem, studies based on random ROIs that encapsulate systematic effects in the LAT data (e.g., imperfect diffuse modeling, unresolved background sources, and percent-level inconsistencies in the IRFs) indicate that the significance estimated by simulations is probably somewhat too high when compared to the asymptotic expectations (Ackermann et al. 2014).

Recalling the discussion in Section 2, sources and ROIs have to be selected such that the overlap is minimal since the joint likelihood function Equation (1) does not account for correlation terms between the different individual likelihood functions. For technical reasons, we cannot define a single ROI containing all 50 clusters, as this leads to an overflow in the number of free parameters that MINOS is not able to handle. We therefore construct non-overlapping ROIs, each containing one or more (non-overlapping) cluster sources.

3.2. Construction of Regions of Interest

In order to avoid overlaps between ROIs, we perform an iterative procedure in which we treat each cluster in our sample with its extension as listed in Table 1 as a seed source and construct a circular region around it. We require these regions to be at least 8° in radius in order to obtain a good fit to the background model. If we cannot accommodate clusters in separate ROIs, we mitigate any remaining overlap by enlarging the ROIs such that more than one cluster may be contained in one analysis region.

Using this method, we are able to construct 26 independent ROIs containing the clusters in our sample which are listed in Table 2. We show the locations and extensions of our selected clusters and the ROIs containing them in Figure 2.

4. SIGNAL AND BACKGROUND MODEL

4.1. Signal Model: Gamma-Ray Emission from Cosmic Rays

In this paper, we focus on the CR-induced γ -ray signal and defer an analysis of γ rays originating from DM decay

⁶³ Both the LAT data as well as the appropriate analysis tools are made available to the public by the *Fermi* Science Support Center <http://fermi.gsfc.nasa.gov/ssc/data/>.

⁶⁴ It should be noted that the binned likelihood analysis using the *Fermi Science Tools* uses square shaped analysis regions. For simplicity, we refer to our ROIs by the central coordinates and radii of the ROI circumcircles.

Table 2
Regions of Interest Considered in This Analysis

| Region | R.A. (°) | Decl. (°) | Radius (°) | Clusters | CC | NCC |
|--------|-------------|--------------|---------------|----------|-----|-----|
| 1 | 12 | -5 | 8 | 2 | 1 | 1 |
| 2 | 15.66 | -21.95 | 8 | 1 | 1 | ... |
| 3 | 354 | -9 | 8 | 2 | 2 | ... |
| 4 | 172.07 | 21.02 | 8 | 1 | ... | 1 |
| 5 | 30.3 | 35.75 | 8 | 1 | 1 | ... |
| 6 | 257.77 | 73.43 | 16 | 2 | ... | 2 |
| 7 | 235 | 27.5 | 8 | 2 | 2 | ... |
| 8 | 259.5 | 40 | 16 | 3 | 3 | ... |
| 9 | 56.57 | 6.48 | 17 | 5 | 4 | 1 |
| 10 | 58.2 | -31.75 | 10 | 2 | 2 | ... |
| 11 | 85.08 | -39.58 | 10 | 2 | ... | 2 |
| 12 | 43.67 | -85.28 | 10 | 1 | 1 | ... |
| 13 | 112.81 | 55.61 | 8 | 2 | ... | 1 |
| 14 | 138.36 | -10.87 | 10 | 2 | 1 | 1 |
| 15 | 159.21 | -27.53 | 8 | 1 | 1 | ... |
| 16 | 321.97 | -60.77 | 16 | 3 | ... | 3 |
| 17 | 316.27 | 1.7 | 8 | 1 | ... | ... |
| 18 | 44.13 | -45.61 | 8 | 1 | 1 | ... |
| 19 | 60 | -58 | 8 | 2 | 1 | 1 |
| 20 | 195.95 | 28.37 | 14 | 2 | 1 | 1 |
| 21 | 349.47 | 15.55 | 16 | 4 | 3 | ... |
| 22 | 197.2 | -18.49 | 8 | 2 | 2 | ... |
| 23 | 360 | -31 | 8 | 3 | 2 | 1 |
| 24 | 17.46 | -45.9 | 8 | 1 | ... | 1 |
| 25 | 68.41 | -13.25 | 8 | 1 | 1 | ... |
| 26 | 87.51 | -25.09 | 8 | 1 | ... | ... |
| Total | | | | 50 | 30 | 16 |

Notes. We group neighboring clusters in non-overlapping analysis regions of interest (ROI) that are defined by center location and the associated radius. Note that with overlap, we refer to the squared counts map inscribed in the circle defined with the coordinates in the table. We list the center of each region along with its radius together with its cluster content. Columns from left to right: ROI ID, R.A. (J2000), decl. (J2000), radius of ROI, number of total clusters in ROI, number of CC-clusters in ROI, and number of NCC-clusters in ROI.

or annihilation to future studies. For a study of γ rays originating from star-forming galaxies in galaxy clusters, see, e.g., Storm et al. (2012). Hydrodynamic simulations of galaxy clusters in a cosmological framework that include CR physics show an approximately universal spectral and spatial CR distribution within clusters as a result of hierarchical structure growth (Pinzke & Pfrommer 2010). The γ -ray emission induced by decaying neutral pions dominates over the inverse Compton emission from primary shock-accelerated electrons or secondaries injected in hadronic CR p - p interactions within clusters (Miniati 2003; Pfrommer et al. 2008; Pinzke & Pfrommer 2010).

Using a very simplified analytic model that employs a CR power-law energy spectrum $dn_{\text{CR}}/d\varepsilon \propto \varepsilon^{-\alpha}$ with spectral index $\alpha = 2$ (i.e., equal CR energy density per logarithmic energy interval), Kushnir & Waxman (2009) claim that the IC emission from primary accelerated electrons at accretion shocks dominates over pion decay γ rays by a factor of $\simeq 150 (\zeta_e/\zeta_p) (kT/10 \text{ keV})^{-1/2}$, where ζ_e and ζ_p denote the fraction of shock-dissipated energy that is deposited in CR electrons and protons, respectively. Instead of the centrally concentrated pion decay emission, this model would give rise to a spatially extended emission reaching out to the accretion shocks beyond the virial radius.

However, there are two simplifying model assumptions that conflict with results from numerical cluster simulations and

observations of non-thermal emission of clusters and supernova remnant shocks, rendering the conclusions about this apparent dominance of the primary inverse Compton emission questionable.

First, the assumed spectral index is in conflict with numerical simulations of cosmological structure formation that have shown a continuous distribution of Mach numbers with weaker flow and merger shocks being more numerous in comparison to strong shocks with Mach numbers exceeding $\mathcal{M} \gtrsim 6$ (Ryu et al. 2003; Pfrommer et al. 2006; Skillman et al. 2008; Vazza et al. 2009, 2011). This necessarily implies a softer effective spectral injection index of primary shock-accelerated particles of $\alpha_{\text{inj}} \simeq 2.3$, which is also consistent with observed spectral indices of radio relics. In fact, elongated relics show a mean radio spectral index of $(\alpha_{\text{v}}) = 1.3$ (Feretti et al. 2012), which translates to a cooling-corrected spectral index of CR electrons of $\alpha = 2\alpha_{\text{v}} = 2.6$ (which is a lower limit since the uncorrected injection index could be as high as $\alpha = 2\alpha_{\text{v}} + 1 = 3.6$). Hence phenomenologically, the relevant shock strengths for radio relic emission are on average characterized by small Mach numbers of $\mathcal{M} \lesssim 3$ and inconsistent with hard CR indices of $\alpha = 2$. It can easily be seen that the different power-law indices are indeed the reason for the strongly differing conclusions on the importance of primary inverse Compton emission. Electrons with an energy of 500 GeV can Compton upscatter CMB photons to γ -ray energies of around 1 GeV. Adopting the effective spectral injection index of primary electrons, $\alpha_{\text{inj}} \simeq 2.3$, and assuming a post-shock temperature at a typical accretion shock of $kT \simeq 0.1 \text{ keV}$, we find a flux ratio of the Kushnir & Waxman (2009) model and that by Pinzke & Pfrommer (2010) of $(500 \text{ GeV}/0.1 \text{ keV})^{0.3 \dots 0.6} \simeq 800 \dots 6 \times 10^5$.

Second, $\zeta_e/\zeta_p \sim 1$ is inconsistent with the observed ratio for Galactic CRs, which has a differential energy ratio of $K_{e/p} \simeq 0.01$ at 10 GeV (Schlickeiser 2002) and observations of supernova remnants constrain the ratio $\zeta_e/\zeta_p \sim 0.001$ (Edmon et al. 2011; Morlino & Caprioli 2012). Assuming universality of the shock acceleration process, statistical inferences about the CR distributions at the solar circle and non-thermal modeling of individual supernova remnants indicate that electron acceleration efficiencies are very subdominant in comparison to that of protons.

Hence, as a baseline model, we apply the simulation-based analytical approach for the CR distribution (Pinzke & Pfrommer 2010), which only requires the gas density profile inferred from X-ray measurements as input. Note that these simulations account only for advective CR transport, where the CRs may be tied to the cluster plasma via small-scale tangled magnetic fields with cored CR profiles as a consequence. Additional CR transport such as CR diffusion and streaming have been neglected. Furthermore, we neglect the potentially important contribution from re-accelerated CRs (e.g., Brunetti & Lazarian 2007, 2011).

The pion decay γ -ray flux above energy E as a result of hadronic CR interactions, $F_{\gamma, \text{exp}}^{\text{CR}}(>E)$, can be parameterized as

$$F_{\gamma, \text{exp}}^{\text{CR}}(>E) = A_{\gamma} \lambda_{\pi^0 \rightarrow \gamma}(>E) \int_V dV \kappa_{\pi^0 \rightarrow \gamma}(R), \quad (3)$$

where the integral extends over the cluster volume V , $\lambda_{\pi^0 \rightarrow \gamma}(>E)$ is the spectral γ -ray distribution, and $\kappa_{\pi^0 \rightarrow \gamma}(R)$ is the spatial distribution, both given in Pinzke & Pfrommer (2010). The parameter, A_{γ} , is a dimensionless universal scale factor, common to all the clusters in the (sub)sample. The predicted γ -ray flux above the minimum energy threshold

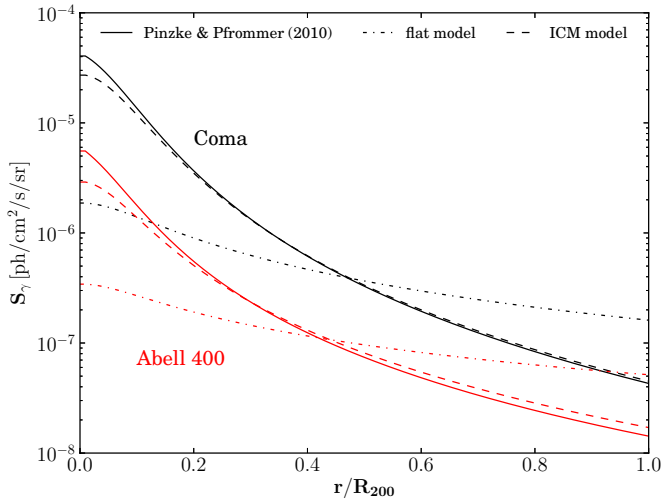


Figure 3. Expected surface brightness profiles for the three spatial models considered in this analysis. We show the profiles for two clusters, Coma (black lines) and A400 (red lines), which have comparable distances ($z = 0.02$) such that the flux difference corresponds to the difference in mass. We note that the ICM model (dashed line) only shows small differences with respect to our simulation-based baseline model (solid line). In contrast, the flat CR pressure model (dashed-dotted line) implies a flattening toward the outskirts of the cluster. (A color version of this figure is available in the online journal.)

500 MeV, $F_{\gamma, \text{exp}}^{\text{CR}} (E > 500 \text{ MeV})$ is calculated using the formalism in Pinzke et al. (2011). We tabulate these values in Table 1. The quoted values of $F_{\gamma, \text{exp}}^{\text{CR}} (E > 500 \text{ MeV})$ correspond to a maximal efficiency $\zeta_{p, \text{max}} = 0.5$ for diffusive shock acceleration of CR ions at structure formation shocks which translate into $A_\gamma = 1$ with correspondingly smaller values of A_γ for smaller efficiencies (obeying however a nonlinear relation). For completeness, we show the CR formalism in Appendix B.

The cluster brightness profile is used to fit the emission from each cluster and is derived from the line-of-sight (l.o.s.) integral of the γ -ray emissivity

$$S_\gamma(\psi, > E) = A_\gamma \lambda_{\pi^0 \rightarrow \gamma}(> E) \times \int_{\Delta\Omega} d\Omega \int_{\text{l.o.s.}} dl \frac{\kappa_{\pi^0 \rightarrow \gamma}(R(l))}{4\pi}, \quad (4)$$

where l is the l.o.s. distance in the direction ψ that the detector is pointing and $R(l) = \sqrt{l^2 + D_a^2 - 2D_a l \cos \Psi}$ is the cluster radius. Here D_a is the angular diameter distance from the Earth to the center of the cluster halo and $\cos \Psi \equiv \cos \theta \cos \psi - \cos \phi \sin \theta \sin \psi$, with θ being the azimuthal angle and ϕ the polar angle. The angular integration $d\Omega = \sin \theta d\theta d\phi$ is performed over a cone centered around ψ . The spatial features of our model are described in more detail in Appendix B.

Outside the very center ($r > 0.03 R_{200}$), this model predicts a rather flat CR-to-thermal pressure profile, i.e., $\langle X_{\text{CR}} \rangle \sim \text{const}$. Most of the emission is contributed from the region around the core radius, which is well outside the central parts. In order to compare the chosen spatial CR profile, we contrast our analysis of the simulation-based model with two additional configurations in which the CR profile is derived from a constant X_{CR} profile (*ICM model*) and a constant P_{CR} profile (*flat model*). The normalizations of these CR profiles are fixed by assuming that the total CR number within R_{200} in our baseline model

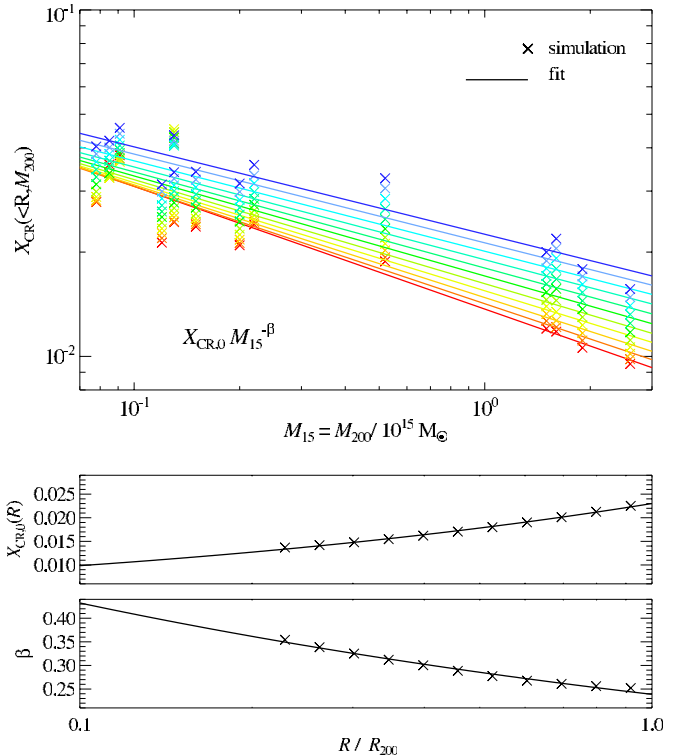


Figure 4. Relative cosmic-ray pressure X_{CR} within radius R . We show the ratio between cosmic-ray pressure and thermal pressure for 14 simulated galaxy clusters with different mass. In the upper panel, the color scheme shows the relative pressure within different radii, in descending order from $1.0 \times R_{200}$ to $0.2 \times R_{200}$ (equally spaced in $\log R$). Each simulated cluster is denoted by a \times and the mass dependence of X_{CR} as a function of radius are denoted by the solid lines. The middle panel shows the radial dependence of the normalization of X_{CR} . The lower panel shows the radial dependence of the slope of the mass dependence of X_{CR} . We find that the relative pressure increases as a function of the radius, but it decreases with increasing cluster mass.

(A color version of this figure is available in the online journal.)

is conserved.⁶⁵ For illustration purposes, we show the surface brightness profiles using our three spatial emission models in Figure 3 for the case of the (massive) Coma cluster and the much less massive cluster A400.

In our framework, the derivation of A_γ also allows us to constrain the CR-to-thermal pressure ratio, X_{CR} , in the ICM using the virial mass and virial radius of each cluster in our sample, since $A_\gamma \propto \langle X_{\text{CR}} \rangle$, where $\langle X_{\text{CR}} \rangle = \langle P_{\text{CR}} \rangle_V / \langle P_{\text{th}} \rangle_V$ and the brackets indicate volume averages. To this end, we make use of the set of 14 galaxy cluster simulations presented in Pinzke & Pfrommer (2010), which span almost two orders of magnitude in mass and include different dynamical states ranging from relaxed to merging clusters. We show the CR-to-thermal pressure ratio X_{CR} as a function of radius and cluster mass in Figure 4. X_{CR} decreases for smaller radius approximately inversely with gas temperature since a composite of CRs and thermal gas favors the gas component over CRs upon adiabatic compression (e.g., Pfrommer & Enßlin 2004a). At a fixed

⁶⁵ Note that CR streaming and diffusion—as spatial transport processes—conserve the total number of CRs. However, outward streaming changes their number density as a function of radius and transforms a peaked CR profile into an asymptotically flat one. Hence, to map an advection-dominated profile (i.e., our simulation-based baseline model) to the corresponding asymptotically flat profile that results from streaming, we compute the volume integral of the number density before and after CR streaming and normalize the latter such that the total number of CRs is conserved.

radius, X_{CR} has a negative trend with mass, that is mainly driven by the virial temperature scaling of the thermal pressure distribution. We have $\langle X_{\text{CR}} \rangle \propto \langle C \rangle / \langle P_{\text{th}} \rangle \propto \tilde{C} / kT_{200} \sim M_{200}^{-0.23}$, where C is the normalization of the CR distribution function and $\tilde{C} = Cm_p/\rho$ denotes the dimensionless normalization, which scales with cluster mass as $\langle \tilde{C} \rangle_V \propto M_{200}^{0.44}$ (Pinzke & Pfrommer 2010) and partially offsets the virial mass scaling of the cluster temperature $kT_{200} \propto M_{200}^{2/3}$.

To formalize these considerations, we fit an empirical relation of $X_{\text{CR}}(R/R_{200}, M_{200})$ to the simulated data points and obtain

$$X_{\text{CR}} = 0.023 A_\gamma \left(\frac{R}{R_{200}} \right)^{0.369} \left(\frac{M_{200}}{10^{15} M_\odot} \right)^{-0.239} \left(\frac{R}{R_{200}} \right)^{-0.258}, \quad (5)$$

where A_γ refers to our universal scale factor derived in the joint likelihood analysis. We tabulate the values for $\langle X_{\text{CR}} \rangle$ for two different integration radii, R_{200} and the half-light radius R_{HL} assuming $A_\gamma = 1$ in Table 1.⁶⁶

4.2. Background Model

The background model for each ROI in this analysis includes templates for the diffuse Galactic and isotropic emission components as well as individual γ -ray sources reported in the 2nd *Fermi*-LAT catalog (Nolan et al. 2012; 2FGL). We model extended 2FGL sources according to the spatial templates provided by the *Fermi* Science Support Center. Unless stated otherwise, we use the standard diffuse and extragalactic γ -ray background templates that are recommended for performing data analysis of reprocessed LAT data.⁶⁷ We note that the Galactic diffuse emission model we use includes a residual component of diffuse γ -ray emission that is not modeled by any template. This component is smoothly varying and does not contribute importantly to the intensity >500 MeV in the regions considered here.⁶⁸

In the background model for each ROI, we include the union of 2FGL sources within the ROI radius enlarged by 5° and 2FGL sources located within 10° of any galaxy cluster in the ROI.

4.3. Free Parameters of the Background Model

Since the average virial radius of clusters in our sample is less than 2° , we leave the normalizations of all sources free that are contained within a 4° radius around each cluster. In addition, we allow the normalization of the templates used to model the Galactic foreground and isotropic diffuse emission to vary freely.

One shortcoming of using the 2FGL catalog (based on 2 yr of LAT observations) to search within a data set covering 4 yr is that spectral parameters (in particular for variable sources) may have substantially changed. To account for this variability, we free the normalization of sources that coincide with bright spatial residuals, and we determine their values through performing a fit using a background-only model to obtain the best-fit for the null-hypothesis.

This procedure produces a large number of free parameters which are then fixed to their maximum likelihood values from the background-only model fit when maximizing the joint

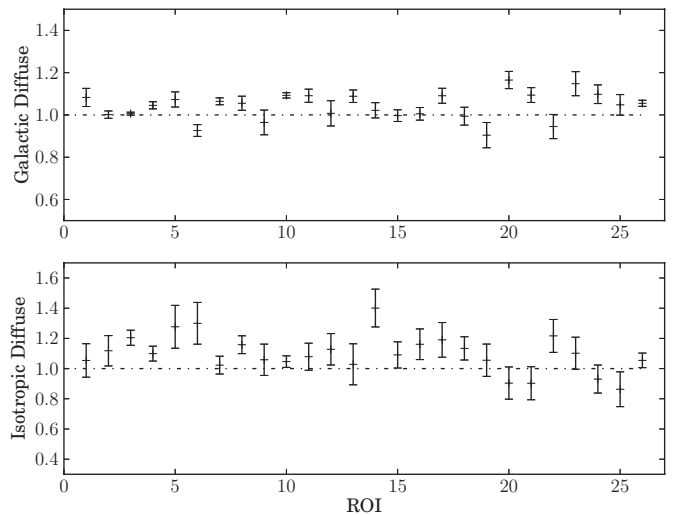


Figure 5. Fit results for the normalization for the Galactic diffuse emission (top) and the isotropic diffuse emission (bottom) in each of the 26 analyzed ROIs. The dot-dashed lines indicate a nominal value of one associated to diffuse templates exactly modeling the emission in the regions. Our regions show a narrow scatter for the Galactic diffuse emission and a slightly larger scatter for the isotropic diffuse component. The latter is also associated with a minor bias toward normalization values >1 .

likelihood function introduced in Section 3.1 in order to avoid an overflow of free parameters and to ensure convergence of the maximization. The normalizations of the Galactic and isotropic diffuse components are left free in each ROI for the joint likelihood fit.

5. RESULTS AND DISCUSSION

We perform our analysis first by treating all 50 clusters in one common set. We call this the combined sample. Recalling the discussion in Section 2, we then separately investigate CC and NCC clusters.

5.1. Background-only Fit

Our ROIs are well described individually by the null hypothesis, i.e., despite the increase in data volume, our results are consistent with emission from only previously detected individual *Fermi*-LAT sources and diffuse emission provided by the Galactic and extragalactic diffuse models, respectively, with the exception of three ROIs: the ROIs containing A400 and, less prominently A1367 and A3112 exhibit residual emission located within the virial radius of each respective cluster. We leave these excesses unmodeled in our baseline analysis and address the interpretation of these residuals in Section 5.3. It is also reassuring that the fitted normalizations of the two global diffuse backgrounds are narrowly scattered around the nominal value of 1 for both the extragalactic (isotropic) and the Galactic diffuse component (refer to Figure 5) across our entire sample. The isotropic component shows a slight bias toward normalizations >1 which however has negligible effect on our results. Figure 6 shows a stacked residual significance map for the full sample and CC and NCC sub-samples. These residual significance maps are created from theoretical model maps of predicted counts from the best-fit null hypothesis model summed over each cluster location. The combined model maps M are then subtracted from the stacked counts maps C from the same region and the residual significance R is computed as $R = (C - M)/\sqrt{M}$. For the

⁶⁶ Here we define the half-light radius as the radius within which half of the emission originates. Note that this radius is usually smaller than $R_{200}/2$.

⁶⁷ For the Galactic diffuse emission, we use the template `g11_iem_v05` and for the isotropic γ -ray background `iso_lean_v05`.

⁶⁸ Further details on this new model can be found on the FSSC Web site.

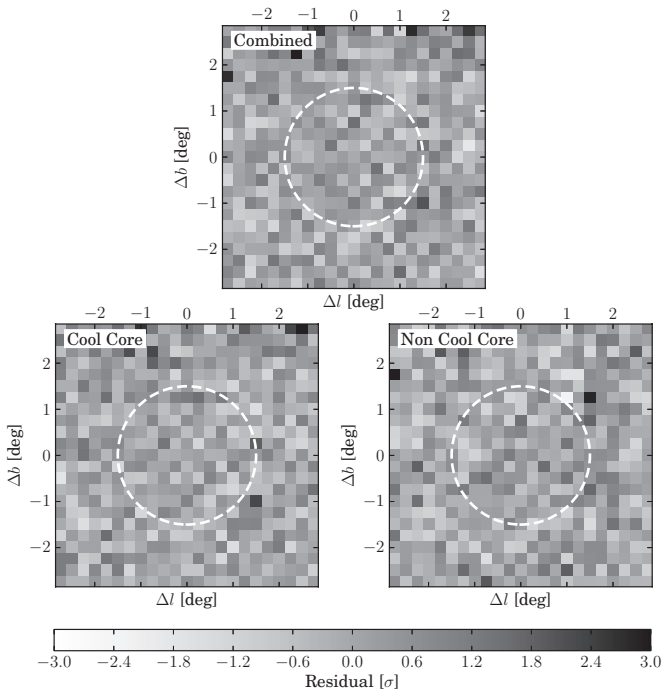


Figure 6. Spatial residual significance maps for the combined sample (top) and the two sub-samples (bottom). The dashed circle corresponds to a radius of 1.5 which covers the majority of the emission region, assuming that the emission is contained within the cluster’s virial radius. The stacked maps are created using the galaxy cluster centers listed in Table 1. We do not observe any significant excess in the combined sample. If observed, any excess in these maps would be extended on at least the scale of the effective point-spread function (PSF) of LAT. Each pixel has a size of 0.25.

spectral residuals, we refer the reader to Appendix E. No obvious excess is visible in either the spectral or spatial residuals.

5.2. Global Significance and Constraints on Common Scale Factor A_γ

We then repeat the fitting procedure including a model of our galaxy clusters with the predicted γ -ray flux $F_{\text{exp}}(E > 500 \text{ MeV})$ and using the spatial template and spectral form proposed by Pinzke et al. (2011), leaving only A_γ to vary freely. We show the distribution of associated TS values for the respective samples in Figure 7.

Assuming that backgrounds are properly modeled, and that CR physics governing the γ -ray emission of clusters is indeed universal, we calculate the best-fit value of the combined scale factor for the full sample along with the two morphological sub-samples. The global TS value of the scale factor for the full sample of 50 clusters is 7.3, corresponding to a 2.7σ evidence. We note that the largest contributors to this signal are however the aforementioned excesses which are spatially coincident with A400 but also less prominently from excesses toward A1367 and A3112. We discuss these special cases in the next section. Removing these clusters from the sample results in a drop of the significance below 2σ , yielding an upper limit to the common scale factor $A_\gamma^{\text{UL}} = 0.29$ at 95% C.L. for the whole cluster sample containing the remaining 47 galaxy clusters. While individually the excess toward A400 yields a higher significance than the excesses toward either A3112 or A1367, in the combined limit, the contribution of this excess becomes negligible due to the lower flux prediction (which mainly determines the weight assigned to each cluster in the

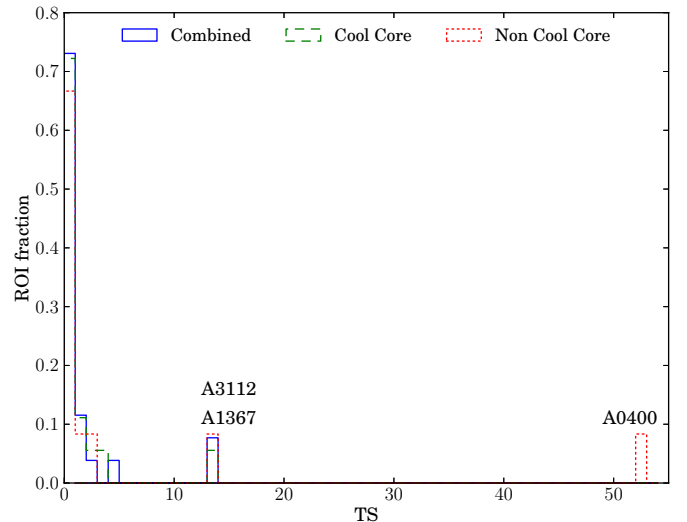


Figure 7. Distribution of ROI TS values for full sample (blue solid line), cool core (red dashed line), and non-cool core (green dash-dotted line). We discuss the notable exceptions with $\text{TS} \geq 9$ in Section 5.3.

(A color version of this figure is available in the online journal.)

Table 3
Joint Scale Factor Limits

| Model | Combined | CC | NCC |
|---------------------------------------|------------|------------|------------|
| Pinzke & Pfrommer (2010) | 0.40 (7.4) | 0.49 (4.7) | 0.44 (2.4) |
| Constant X_{CR} (ICM model) | 0.48 (7.2) | 0.64 (4.9) | 0.49 (2.4) |
| Constant P_{CR} (flat model) | 1.78 (9.7) | 3.02 (5.2) | 1.71 (5.0) |

Notes. Summary of joint scale factors. Columns 2–4 indicate the 95% upper limit on the joint scale factor A_γ for the respective samples. The global TS values of each setup and sample are given in brackets.

joint analysis), as compared to, e.g., the contribution from Coma that dominates the upper limit.

Since at present we can neither claim nor refute the origin of the observed excesses being due to γ rays from the ICM, we calculate upper limits on the universal scaling factor, leaving those respective excesses unmodeled. For our whole sample, we find a combined limit of $A_\gamma^{\text{UL}} = 0.41$ at 95% C.L. Considering the NCC/CC subsamples, we find weaker limits $A_\gamma^{\text{UL}} = 0.47$ on the scale factor for NCC systems as compared to $A_\gamma^{\text{UL}} = 0.49$ for the CC subsample.

We also calculated the limit on the combined scale factor for our two alternative spatial CR profiles. For the ICM model, we obtain $A_\gamma^{\text{UL}} = 0.48$, and for the flat model, the combined limit is roughly a factor of four larger with respect to the results from the baseline model, yielding $A_\gamma^{\text{UL}} = 1.78$, at 95% C.L. The associated global TS values are 7.2 and 9.7, respectively.⁶⁹ In addition, a flat CR profile is preferred in the case of the Coma cluster which is also the cluster that contributes most to the constraints in the NCC cluster subsample. We provide the final values for our three setups in Table 3.

For the combined sample, we exclude $A_\gamma = 1$ at more than a 5σ confidence level, while for CC/NCC, it is excluded at more than a 4σ confidence level.

⁶⁹ Removing A400, A1367, and A3112 from the cluster sample yields smaller global TS values of 2.8 for the ICM model and 4.7 for the flat model, respectively.

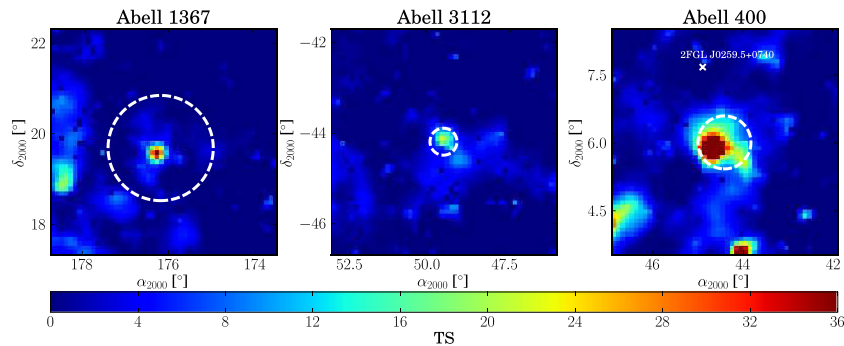


Figure 8. TS maps from an unbinned search in a $5^\circ \times 5^\circ$ region centered on each of our notable clusters, A1367, A3112, and A400. All excesses are found within the assumed cluster virial radius (dashed white circle), albeit marginally offset from the respective cluster centers (0.3 for both A400 and A1367 and 0.1 for A3112). Each pixel has a width of 0.1 . The white \times indicates the best-fit position of a previously detected 2FGL point source.

(A color version of this figure is available in the online journal.)

Table 4
Best-fit Positions of Excess Emission

| Host Cluster | R.A. ($^\circ$) | Decl. ($^\circ$) | r_{68} ($^\circ$) |
|--------------|----------------------|-----------------------|--------------------------|
| A0400 | 44.68 | 5.86 | 0.03 |
| A1367 | 176.25 | 19.54 | 0.04 |
| A3112 | 49.56 | -44.22 | 0.02 |

Notes. We report the best-fit positions from our refined search using the `gttsmap` tool that employs a maximum likelihood analysis in order to localize a new point source. The columns from left to right: name of the host cluster, R.A. (J2000), decl. (J2000), and uncertainty (r_{68}). All values are given in degrees.

5.3. The Case of A1367, A3112, and A400

We obtained a TS value of 13.8, corresponding to a pre-trial factor significance of 3.7σ individually for each of the candidate γ -ray sources at the locations of A1367 (Leo cluster) and A3112. Conservatively, assuming a binomial distribution for the trial probability, we find that these excesses correspond to a post-trial significance of 2.6σ . For each of these regions, we calculated a TS map using an unbinned likelihood method in a $5^\circ \times 5^\circ$ region centered around each cluster with a grid spacing of 0.1 between test positions. The TS value of a putative point-like source with a hadronic CR spectrum is evaluated at each test position on the grid to create a spatial map of the excess emission. We show these TS maps in Figure 8.

In both cases, we find that the excess emission, albeit marginally offset from the center of the cluster (0.3 for A1367 and 0.1 for A3112) is still contained within the virial radius of the respective cluster. For A1367 the difference in TS obtained at the center of the cluster and the peak TS position as shown in Figure 8 is 15, while for A3112 the offset is smaller than the

resolution used to create the TS maps. In order to test whether the emission is more appropriately modeled assuming an extended emission profile over a new point source, we follow the analysis presented in Lande et al. (2012), which gauges the spatial extent of the source by taking the difference, TS_{ext} between the TS for a point source signal hypothesis and the extended source signal hypothesis. Lande et al. (2012) found that sources with $TS_{\text{ext}} > 16$ are confidently ascertained to be spatially extended beyond the LAT point-spread function (PSF).⁷⁰ For A1367 and A3112, we find $TS_{\text{ext}} = 2.6$ and $TS_{\text{ext}} = 0.9$, respectively. Assuming that the excesses toward all three clusters constitutes point-like emission, we first obtained a better estimate for the location of the excess using the `gtfindsrc` tool and then repeated the calculation of TS maps using a finer binning of 0.02 . We report the best-fit values of these excesses along with their uncertainties in Table 4.

We also investigate the spectral behavior of the excesses toward A1367 and A3112, by replacing the hadronic CR spectrum with a featureless power-law, such that the flux becomes:

$$F_{\gamma}^{\text{PL}}(E) = A_{\gamma} \times F_{\gamma, \text{exp}}^{\text{CR}}(>500 \text{ MeV}) \times \frac{(1 - \Gamma) \times E^{-\Gamma}}{E_{\text{max}}^{1-\Gamma} - E_{\text{min}}^{1-\Gamma}}, \quad (6)$$

where Γ is the spectral index and $E_{\text{min}} = 500 \text{ MeV}$ and $E_{\text{max}} = 200 \text{ GeV}$ correspond to the energy range of the analysis. $F_{\gamma, \text{exp}}^{\text{CR}}(E > 500 \text{ MeV})$ denotes the expected integral flux above E_{min} . A_{γ} corresponds to the scale factor introduced in Section 5.2. For this test, we leave both A_{γ} and Γ free to vary. We report the best-fit values of these parameters in Table 5.

For both A1367 and A3112, we find that harder spectral indices are preferred over softer, with a best-fit value for

⁷⁰ In Lande et al. (2012), the authors used a disk to perform their studies.

Table 5
Spectral Model Comparison

| Cluster | A_{γ} (Hadronic Model) | TS (Hadronic Model) | A_{γ} (Power Law) | Γ (Power Law) | TS_{PL} (Power Law) |
|---------|----------------------------------|------------------------|-----------------------------|-------------------------|---------------------------------|
| A1367 | 3_{-1}^{+2} | 13.8 | 1.7 ± 0.9 | 1.7 ± 0.3 | 17.3 |
| A3112 | 3 ± 2 | 13.8 | 2.0 ± 1.5 | 1.7 ± 0.4 | 16.1 |
| A400 | 39_{-10}^{+11} | 52.7 | 43 ± 8 | 2.3 ± 0.2 | 52.8 |

Notes. Spectral model comparison of clusters that exhibit excess emission. Shown are the best-fit values for A_{γ} along with their associated TS values for the hadronic model and the corresponding values for A_{γ} when replacing the spectrum by a featureless power-law of index Γ , given by Equation (6). The last column indicates the obtained TS value with the power-law fit.

$\Gamma = 1.7 \pm 0.3$ and $\Gamma = 1.7 \pm 0.4$, for A1367 and A3112, respectively.

While none of the aforementioned tests decisively exclude the attribution of the observed excesses to CR-induced γ -ray emission from the ICM, we note that both A3112 and A1367 are hosts to head-tail radio sources which may be the source of the observed γ -ray emission (see, e.g., Gavazzi & Jaffe 1982, 1987 for A1367 and Costa & Loyola (1998) for A3112). A discussion of supporting multifrequency arguments is given in Appendix D.

The excess found in A400 yields a TS value of 52.7 which nominally corresponds to a significance of 7.3σ pre-trial (6.7σ post-trial). We performed the same tests as in the case of A1367 and A3112 and find that the excess is contained within the cluster virial radius, although the TS map indicates that the emission is about 0.3 offset from the cluster center. The difference between the TS evaluated at the cluster center and at the position of the excess is 38. The test for extendedness (centered at the cluster center) yields $TS_{\text{ext}} = 15.0$, indicating a preference for an extended source, which is likely explained by the offset of the excess. This casts further doubt on the explanation of the excess being ICM emission that moreover would be concentrated toward the cluster center. Fitting the excess with a power-law spectral model as in the case of A3112 and A1367 yields a best-fit value for $\Gamma = 2.3 \pm 0.2$ and $A_\gamma = 43 \pm 8$ with an associated TS value of 52.8, which is similar to that obtained for the hadronic model.

In addition to these tests, we searched for source variability using aperture photometry and found no indications of variability on time scales of one month. We note, however, that the obtained scale factor for A400, $A_\gamma = 39^{+11}_{-10}$, is in strong tension with baseline model expectations and the scale factor constraints derived from other clusters in our sample. If the excess toward A400 constitutes a signal, the calculated upper limit from A400 corresponds to the usual statement that scale factors larger than the upper limit are inconsistent with the data on the stated confidence level. If the excess instead stems from the unmodeled background, then the upper limit means that scale factors larger than the upper limit would make the model more inconsistent with the data than the background-only hypothesis allows at the stated confidence level. In both cases, the result is a conservative upper limit and in addition (as mentioned in Section 5.2) A400 does not affect the combined upper limit sizeably. Removing A400 from the sample yields a marginally stronger upper limit on the common scale factor for the combined sample of the remaining 49 clusters of $A_\gamma^{\text{UL}} = 0.40$.

In the conservative CR model of Pinzke & Pfrommer (2010), $A_\gamma = 1$ corresponds to a pion decay γ -ray flux owing to CR protons accelerated at structure formation shocks with a maximal acceleration efficiency and neglecting active CR transport.⁷¹ Allowing for CR streaming transport would cause a net CR flux to the dilute outer cluster regions and would reduce the γ -ray yield for that acceleration efficiency. Additionally, Pinzke & Pfrommer (2010) presented an optimistic CR model including effects which enhance the predicted γ -ray yield by a factor of 2–3 depending on the cluster mass.⁷² However, that model does not account for CRs that are injected by AGNs

over the cluster lifetime, which could also produce pions in inelastic collision with the ICM. The total energy dissipation by gravitational shocks exceeds that of AGNs for large clusters, making it unlikely that AGN-injected CRs dominate the diffuse γ -ray signal. However, this argument does not apply for smaller CCs (in particular in their central cluster regions) where the AGN appears to dominate the energy budget and could possibly also give rise to observable γ -ray emission (see, e.g., Pfrommer 2013, for the interpretation of the low-state of M87 in terms of diffuse pion decay emission while the high state is attributed to jet-induced emission). Hence, the most likely explanation for the possible signal with $A_\gamma \simeq 39$ in A400 is jet-related emission from point sources projected onto or within the cluster. A potential source for the emission in A400 may be the quadruple head-tail system 3C 75 which also shows X-ray core emission in the galaxies (Owen et al. 1985; Hudson et al. 2006). However, given that 3C 75 is located toward the center of A400 and the excess is 0.3 offset, which is about eight times larger than the 68% error radius for a pointsource, this possibility is unlikely.

5.4. Individual Upper Limits on the γ -ray Flux

Assuming that each cluster in our sample can be modeled according to our description in Section 4.1, one can also derive *individual* limits on $A_{\gamma,i}$ where i refers to the individual cluster. These individual limits can be propagated into flux limits.

In addition, in order to assess the impact of modeling the clusters in our sample as extended sources, we have derived individual flux upper limits modeling the clusters as point sources.

In Figure 9, we show these two cases, contrasting the individually derived γ -ray flux limits for extended emission from those derived when assuming the cluster emission to be point-like. We tabulate the former for various energy bands along with their associated (pre-trial) TS values in Table 6. We note that the limit on A_γ , derived from the Coma cluster alone is comparable to the jointly derived limit from the full sample of all 50 clusters in this study, emphasizing its weight in the joint analysis. We investigated the potential dependence of the upper limits on the Galactic diffuse emission model. In the great majority of cases the limits vary by less than 30% for the range of models that we considered. Those clusters for which the dependence on the model was more sensitive are marked in Table 6. However, this sensitivity does not affect the combined limit.

In Figure 10, we show individual γ -ray flux upper limits that are derived for the CR profile following: (1) a constant X_{CR} profile (ICM model) and (2) a constant P_{CR} profile (flat model). We tabulate these values along with their (pre-trial) TS values in Table 7. We find that the limits derived from the first model are very similar to those with our simulation-based model. On the other hand, the flat model (i.e., constant CR pressure profile) yields less stringent upper limits. We also note that the associated TS values for the flat CR profile are generally marginally higher than either those derived from the thermal ICM or our simulation-based approach. This is expected since the choice of a flat CR profile yields a substantially flatter γ -ray surface brightness profile, which in turn provides a better fit to the data compared to a cored profile, in particular, when considering that the excess emission we report in the previous section is offset from the cluster center. We also note that from the three excesses found, only those toward A3112 and A400 remain with $TS > 9$ when using the flat CR profile instead.

The flux limits we derive substantially improve over previous limits (Ackermann et al. 2010b) due to the increase in data

⁷¹ The acceleration efficiency that was used in the simulations was based on observations of supernova remnants and theoretical calculations of diffusive shock acceleration. It is unlikely that there are more efficient mechanisms at work.

⁷² A part of the enhancement was due to the numerical limitation of smoothed particle hydrodynamics to excite Kelvin–Helmholtz instabilities and fully mix a ram-pressure stripped interstellar medium into the ICM.

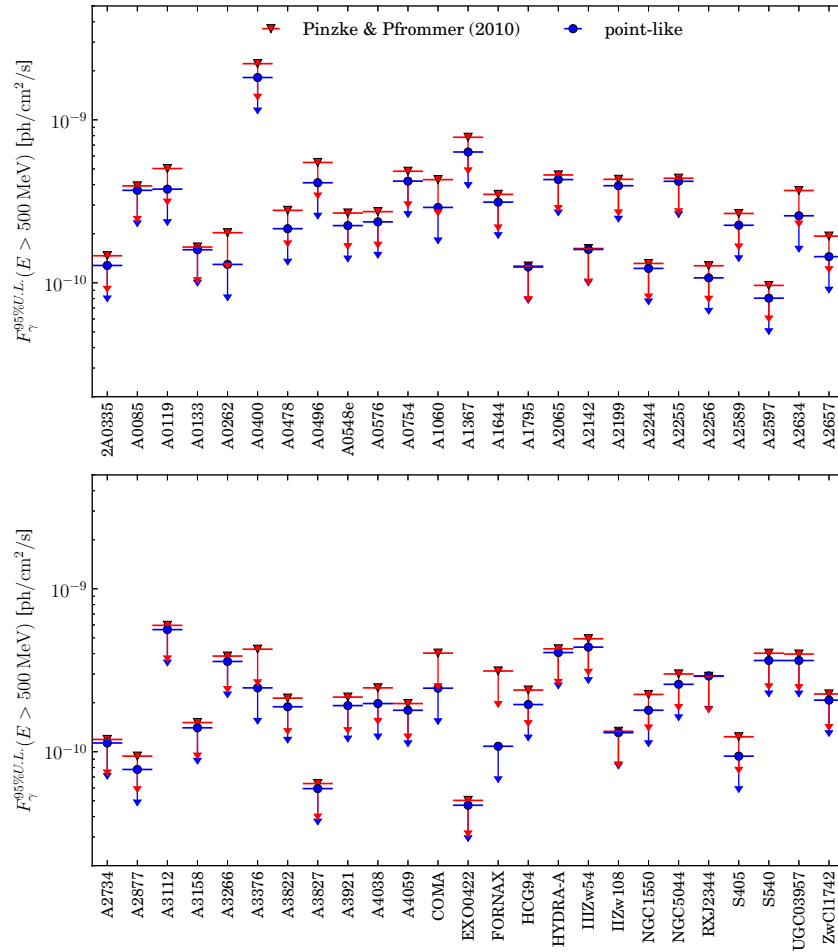


Figure 9. Shown are the 95% upper limits on hadronic CR-induced γ -ray flux for each of our 50 galaxy clusters in this analysis. We show the *individually* derived upper limits for both the extended emission (red downward triangle) and assuming the cluster emission to be point-like (blue circle). (A color version of this figure is available in the online journal.)

volume and improved modeling of the γ -ray sky as well as improved instrument understanding reflected by the use of reprocessed LAT data with on-orbit calibrations. Finally, we note that in particular for spatially extended clusters such as Coma or Fornax, the limits are substantially weakened with respect to when modeling them as point-like objects.

Motivated by the *Fermi*-LAT detection of few bright cluster galaxies (e.g., 2FGL J0627.1–3528 in A3392 and 2FGL J1958.4–3012 in RXC J1958–3011), a recent stacking study by Dutson et al. (2013) investigated a large sample of galaxy clusters that was selected according to the radio flux of bright cluster galaxies. Although based on a different scientific prior and methodology than our cluster analysis, the determined flux limits can be compared to the point-source upper limits reported here. About a dozen clusters are in common between both studies. However, Dutson et al. (2013) used the respective coordinates of the bright cluster galaxy, which are not necessarily consistent with the cluster center coordinates considered in our studies. Given the LAT PSF (Bregeon et al. 2013) and the considered ROIs this does not constitute a severe handicap for comparison. The use of different exposures (45 months in Dutson et al. 2013 and 48 months in this work), the use of different source models, and, perhaps most particularly noteworthy, the use of reprocessed LAT data with associated different Galactic and isotropic diffuse models (`gal_2yearp7v6_v0` versus `gll_iem_v05` and `iso_p7v6source` versus `iso_clean_v05`

respectively), as well as different analysis energy thresholds, render a strict comparison more problematic. For the majority of common clusters, the limits in Dutson et al. (2013) are marginally less sensitive, as expected regarding the slightly less exposure and the rather moderate changes in the diffuse background models.

However, there are two noticeable exceptions: A85 and A2634 appear to have more constraining upper limits in Dutson et al. (2013), besides less exposure and a lower analysis threshold. The discrepancies could be explained by differences in the construction of the ROI (treatment of variable sources, sources to be too faint to be in the 2FGL catalog, size of ROI). Taking the respective flux limits at face value, the differences do not amount to more than 35% between both studies. Our limits on extended cluster emission cannot be meaningfully compared to the point-source upper limits in Dutson et al. (2013) as they constitute alternative scientific priors for a different scientific problem. However, our individual limits on the γ -ray flux, while being specifically derived within the framework of the universal CR model by Pinzke & Pfrommer (2010), can, in principle, be used to constrain other classes of models.

5.5. CR-to-Thermal Pressure Ratio (X_{CR})

We show the resulting upper limits on the CR-to-thermal pressure ratio, $\langle X_{\text{CR}} \rangle$ in Figure 11. These numbers were obtained by scaling the $\langle X_{\text{CR}} \rangle$ values in Table 1 with the limit on A_{γ}

Table 6
Individual Flux Upper Limits

| Cluster | $A_{\gamma,i}^{\text{UL}}$ | $F_{\gamma,500\text{MeV}}^{\text{UL}}$ | $F_{\gamma,1\text{GeV}}^{\text{UL}}$ | $F_{\gamma,10\text{GeV}}^{\text{UL}}$ | TS | $A_{\gamma,i}^{\text{UL}}$ | $F_{\gamma,500\text{MeV}}^{\text{UL}}$ | $F_{\gamma,1\text{GeV}}^{\text{UL}}$ | $F_{\gamma,10\text{GeV}}^{\text{UL}}$ | TS |
|--------------------|----------------------------|--|--------------------------------------|---------------------------------------|----------|----------------------------|--|--------------------------------------|---------------------------------------|------------|
| | Extended | Extended | Extended | Extended | Extended | Point-like | Point-like | Point-like | Point-like | Point-like |
| 2A0335 | 0.52 | 1.5 | 6.7 | 3.6 | 0.0 | 0.45 | 1.3 | 5.9 | 3.1 | 0.0 |
| A0085 | 1.35 | 3.9 | 18.0 | 9.5 | 1.0 | 1.26 | 3.7 | 16.9 | 9.0 | 1.3 |
| A0119 | 3.54 | 5.0 | 23.0 | 12.2 | 2.7 | 2.65 | 3.8 | 17.2 | 9.1 | 0.8 |
| A0133 | 2.32 | 1.7 | 7.6 | 4.0 | 0.0 | 2.23 | 1.6 | 7.3 | 3.9 | 0.0 |
| A0262 | 1.67 | 2.0 | 9.3 | 4.9 | 0.0 | 1.07 | 1.3 | 5.9 | 3.1 | 0.0 |
| A0400 | 50.11 | 22.2 | 101.7 | 53.6 | 52.7 | 41.20 | 18.3 | 83.6 | 44.1 | 37.7 |
| A0478 ^a | 1.14 | 2.8 | 12.7 | 6.7 | 0.0 | 0.88 | 2.1 | 9.8 | 5.2 | 0.0 |
| A0496 ^a | 1.94 | 5.5 | 25.2 | 13.3 | 1.9 | 1.46 | 4.1 | 18.9 | 10.0 | 0.5 |
| A0548e | 10.78 | 2.7 | 12.3 | 6.5 | 0.1 | 9.02 | 2.2 | 10.3 | 5.4 | 0.0 |
| A0576 | 4.39 | 2.7 | 12.6 | 6.6 | 0.2 | 3.80 | 2.4 | 10.9 | 5.7 | 0.3 |
| A0754 | 2.86 | 4.8 | 22.2 | 11.7 | 1.1 | 2.49 | 4.2 | 19.3 | 10.2 | 0.7 |
| A1060 | 1.89 | 4.3 | 19.7 | 10.4 | 0.4 | 1.28 | 2.9 | 13.3 | 7.0 | 0.1 |
| A1367 | 4.08 | 7.8 | 35.9 | 19.0 | 13.8 | 3.31 | 6.4 | 29.1 | 15.4 | 11.2 |
| A1644 | 2.69 | 3.5 | 16.0 | 8.5 | 0.2 | 2.41 | 3.1 | 14.3 | 7.6 | 0.4 |
| A1795 ^a | 0.42 | 1.3 | 5.8 | 3.1 | 0.0 | 0.42 | 1.3 | 5.7 | 3.0 | 0.0 |
| A2065 | 5.00 | 4.6 | 21.1 | 11.2 | 2.3 | 4.69 | 4.3 | 19.8 | 10.5 | 2.2 |
| A2142 | 0.47 | 1.6 | 7.4 | 3.9 | 0.0 | 0.46 | 1.6 | 7.3 | 3.9 | 0.0 |
| A2199 | 1.45 | 4.3 | 19.8 | 10.5 | 1.9 | 1.32 | 4.0 | 18.1 | 9.6 | 1.7 |
| A2244 | 1.74 | 1.3 | 6.0 | 3.2 | 0.0 | 1.63 | 1.2 | 5.6 | 3.0 | 0.0 |
| A2255 | 5.21 | 4.4 | 20.2 | 10.6 | 5.2 | 4.99 | 4.2 | 19.3 | 10.2 | 6.3 |
| A2256 | 0.50 | 1.3 | 5.8 | 3.1 | 0.0 | 0.42 | 1.1 | 4.9 | 2.6 | 0.0 |
| A2589 ^a | 3.96 | 2.7 | 12.2 | 6.5 | 0.0 | 3.36 | 2.3 | 10.4 | 5.5 | 0.0 |
| A2597 | 1.27 | 1.0 | 4.4 | 2.3 | 0.0 | 1.06 | 0.8 | 3.7 | 2.0 | 0.0 |
| A2634 | 5.95 | 3.7 | 17.0 | 8.9 | 0.3 | 4.16 | 2.6 | 11.9 | 6.2 | 0.0 |
| A2657 ^a | 2.34 | 1.9 | 8.9 | 4.7 | 0.0 | 1.75 | 1.4 | 6.6 | 3.5 | 0.0 |
| A2734 | 2.71 | 1.2 | 5.5 | 2.9 | 0.0 | 2.58 | 1.1 | 5.2 | 2.7 | 0.0 |
| A2877 | 1.87 | 0.9 | 4.3 | 2.3 | 0.0 | 1.55 | 0.8 | 3.6 | 1.9 | 0.0 |
| A3112 | 5.37 | 6.0 | 27.3 | 14.4 | 13.8 | 5.06 | 5.6 | 25.7 | 13.6 | 12.8 |
| A3158 | 1.26 | 1.5 | 6.9 | 3.7 | 0.0 | 1.17 | 1.4 | 6.4 | 3.4 | 0.0 |
| A3266 | 1.24 | 3.9 | 17.7 | 9.4 | 2.2 | 1.15 | 3.6 | 16.4 | 8.7 | 3.6 |
| A3376 | 6.20 | 4.3 | 19.5 | 10.3 | 0.0 | 3.59 | 2.5 | 11.3 | 6.0 | 0.0 |
| A3822 | 4.77 | 2.1 | 9.8 | 5.2 | 0.0 | 4.22 | 1.9 | 8.7 | 4.6 | 0.0 |
| A3827 | 0.66 | 0.6 | 2.9 | 1.5 | 0.0 | 0.61 | 0.6 | 2.7 | 1.4 | 0.0 |
| A3921 ^a | 4.63 | 2.2 | 9.9 | 5.2 | 0.1 | 4.11 | 1.9 | 8.8 | 4.6 | 0.0 |
| A4038 | 1.84 | 2.5 | 11.3 | 6.0 | 0.1 | 1.48 | 2.0 | 9.1 | 4.8 | 0.0 |
| A4059 | 2.04 | 2.0 | 9.1 | 4.8 | 0.0 | 1.86 | 1.8 | 8.2 | 4.4 | 0.0 |
| COMA ^a | 0.35 | 4.0 | 18.5 | 9.8 | 0.7 | 0.22 | 2.5 | 11.3 | 6.0 | 0.1 |
| EXO0422 | 0.70 | 0.5 | 2.3 | 1.2 | 0.0 | 0.65 | 0.5 | 2.2 | 1.1 | 0.0 |
| FORNAX | 3.73 | 3.1 | 14.3 | 7.6 | 0.0 | 1.29 | 1.1 | 4.9 | 2.6 | 0.0 |
| HCG94 | 6.34 | 2.4 | 11.0 | 5.8 | 0.0 | 5.17 | 2.0 | 9.0 | 4.7 | 0.0 |
| HYDRA-A | 2.57 | 4.3 | 19.6 | 10.4 | 3.1 | 2.44 | 4.1 | 18.6 | 9.8 | 3.2 |
| IIIZw54 | 10.97 | 5.0 | 22.7 | 12.0 | 0.5 | 9.74 | 4.4 | 20.2 | 10.6 | 0.3 |
| IIZw108 | 3.31 | 1.3 | 6.1 | 3.2 | 0.0 | 3.25 | 1.3 | 6.0 | 3.2 | 0.0 |
| NGC 1550 | 3.37 | 2.3 | 10.3 | 5.5 | 0.0 | 2.70 | 1.8 | 8.3 | 4.4 | 0.0 |
| NGC 5044 | 4.96 | 3.0 | 13.8 | 7.3 | 0.0 | 4.29 | 2.6 | 11.9 | 6.3 | 0.0 |
| RXJ2344 | 5.07 | 2.9 | 13.3 | 7.0 | 1.3 | 5.10 | 2.9 | 13.4 | 7.1 | 2.3 |
| S405 ^a | 3.11 | 1.2 | 5.7 | 3.0 | 0.0 | 2.36 | 0.9 | 4.3 | 2.3 | 0.0 |
| S540 | 11.47 | 4.0 | 18.5 | 9.7 | 1.2 | 10.35 | 3.6 | 16.7 | 8.8 | 0.8 |
| UGC03957 | 8.00 | 4.0 | 18.2 | 9.6 | 0.4 | 7.31 | 3.6 | 16.6 | 8.8 | 0.3 |
| ZwCl1742 | 1.94 | 2.3 | 10.4 | 5.5 | 0.0 | 1.77 | 2.1 | 9.5 | 5.0 | 0.0 |

Notes. The columns contain from left to right the 95% upper limit on $A_{\gamma,i}$ for each cluster, the derived flux upper limit above (500 MeV, 1 GeV, and 10 GeV), the associated TS value as well as the same quantities assuming the clusters to be modeled by a point source at the cluster position as given in Table 1. Fluxes are given in $\text{photon s}^{-1} \text{cm}^{-2}$.

^a The upper limits on $A_{\gamma,i}$ derived using our alternative diffuse models (Section 6.3) for these clusters varied by more than 30% relative to those obtained using the standard diffuse emission model.

from Section 5.2. This procedure assumes universality of the CR distribution as suggested by hydrodynamical cosmological simulations of clusters (Pinzke & Pfrommer 2010) and implicitly asserts that the active CR transport does not appreciably modify the spatial distribution of the CRs. This is justified since the impact of CR streaming on the CR distribution of a cosmo-

logical cluster is not clear to date. Depending on the microscopic plasma physics that sets the CR streaming speed (i.e., competing damping mechanisms of the CR Alfvén waves) and the macroscopic distribution of cluster magnetic fields (Pfrommer & Dursi 2010; Ruszkowski et al. 2011, for evidence of radial bias of the magnetic geometry), CR streaming could either be a

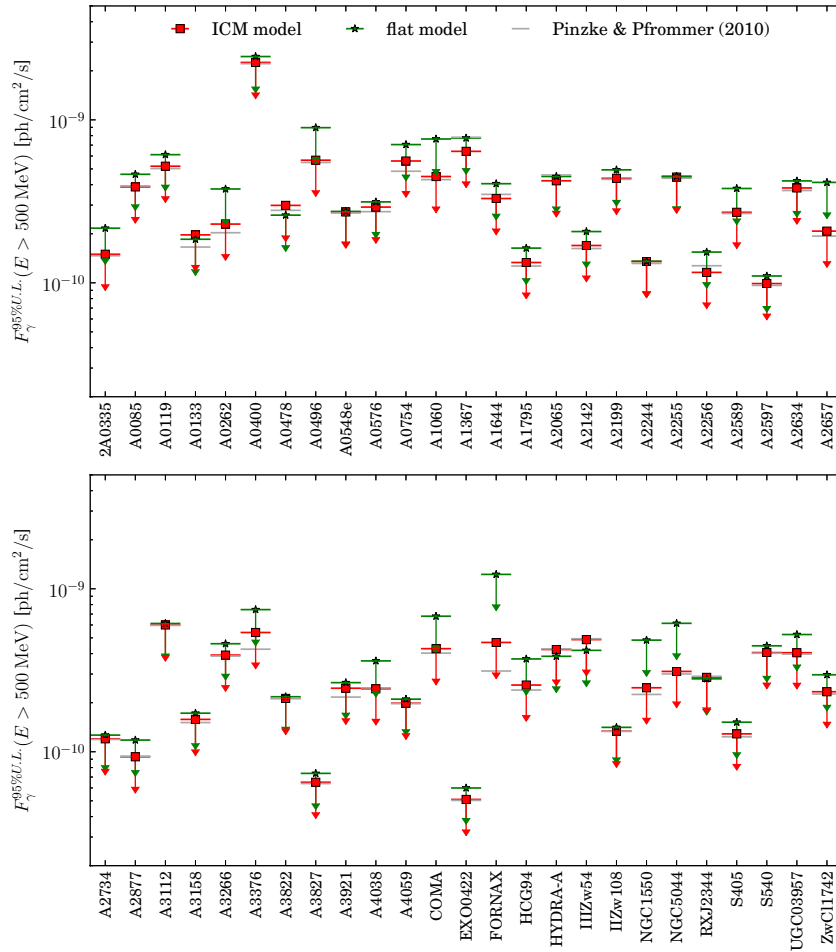


Figure 10. Same as Figure 9 but for spatial CR profiles following a constant X_{CR} profile (ICM model, red squares) and a constant P_{CR} profile (flat model, green stars). To allow for an easier comparison, we show the limits from the baseline analysis (Figure 9) in horizontal gray lines. (A color version of this figure is available in the online journal.)

perturbation to the peaked advection-dominated CR distribution or cause a substantial flattening by a substantial net outward CR flux (Enßlin et al. 2011; Wiener et al. 2013).

The median upper limit on the CR pressure ratio is $\langle X_{\text{CR}} \rangle < 0.006$ for the combined sample and the NCC subsample within R_{HL} . Those constraints are relaxed to $\langle X_{\text{CR}} \rangle < 0.012$ (combined sample) and $\langle X_{\text{CR}} \rangle < 0.013$ (NCC) within R_{200} . For CC clusters, this limit is less stringent, yielding $\langle X_{\text{CR}} \rangle < 0.008$ and $\langle X_{\text{CR}} \rangle < 0.014$ within R_{HL} and R_{200} , respectively.

These limits are more constraining than the previous limits on the CR pressure that were obtained through flux upper limits on individual objects; in particular, they are constraining for individual limits on clusters using the initial 18 months of LAT data (Ackermann et al. 2010b); also, the limits improve those constraints that use four years of *Fermi* data on Coma, which yield $\langle X_{\text{CR}} \rangle < 0.017$ (Arlen et al. 2012), provided the CR universality assumption holds.⁷³ The most suitable cluster target for CR-induced γ -ray emission, the Perseus cluster, cannot be used to competitively constrain the CR pressure using *Fermi*-LAT data since the *Fermi*-LAT and MAGIC collaborations detected the central radio galaxy NGC 1275 in γ rays in the energy range from 300 MeV to > 300 GeV (*Fermi*: 300 MeV–300 GeV, MAGIC: > 200 GeV) (Abdo et al. 2009; Aleksić et al. 2012b).

⁷³ Assuming both universality as well as the scaling relation we adopt throughout our work, which is characterized through A_γ for the combined sample, for Coma, we find $\langle X_{\text{CR}} \rangle < 0.011$.

Non-observations of γ rays from the Perseus cluster *above* these energies by the MAGIC Collaboration (Aleksić et al. 2012a, 2010b) provide limits similar to those obtained from analyzing LAT observations of Coma, $\langle X_{\text{CR}} \rangle < 0.017$ alone (Arlen et al. 2012; Zandanel & Ando 2013).

Our limits on X_{CR} probe the entire ICM and are much more constraining in comparison to the limits on the non-thermal pressure contribution of the central ICM in several nearby cD galaxies that have been derived by comparing the gravitational potentials inferred from stellar and globular cluster kinematics and from assuming hydrostatic equilibrium of the X-ray emitting gas (Churazov et al. 2008, 2010). Depending on the adopted estimator of the optical velocity dispersion, they find a non-thermal pressure bias of $X_{\text{nt}} = P_{\text{nt}}/P_{\text{th}} \approx 0.21$ –0.29, which probes the cumulative non-thermal pressure contributed by CRs, magnetic fields, and unvirialized motions. It is, however, conceivable that those central regions of CC clusters, which probe the enrichment of non-thermal components as a result of AGN feedback (e.g., Pfrommer 2013), are characterized by a larger CR pressure contribution in comparison to the bulk of the ICM that probes CRs accelerated by shocks associated with the growth of structure and magnetic fields that are reprocessed by these shocks.

Complementary limits on CRs are also derived from radio (synchrotron) observations (Pfrommer & Enßlin 2004a; Brunetti et al. 2007). Assuming a central cluster magnetic

Table 7
Individual Flux Upper Limits (Alternative CR Profiles)

| Cluster | $A_{\gamma,i}^{\text{UL}}$ | $F_{\gamma,\text{exp}}^{\text{CR}}$ | $F_{\gamma,500\text{MeV}}^{\text{UL}}$ | TS | $A_{\gamma,i}^{\text{UL}}$ | $F_{\gamma,\text{exp}}^{\text{CR}}$ | $F_{\gamma,500\text{MeV}}^{\text{UL}}$ | TS |
|---------------|----------------------------|-------------------------------------|--|------|----------------------------|-------------------------------------|--|------|
| Spatial Model | ICM | ICM | ICM | ICM | Flat | Flat | Flat | Flat |
| 2A0335 | 0.85 | 1.8 | 1.5 | 0.0 | 5.14 | 0.4 | 2.2 | 0.0 |
| A0085 | 1.64 | 2.4 | 3.9 | 0.6 | 6.15 | 0.8 | 4.6 | 1.1 |
| A0119 | 3.91 | 1.3 | 5.2 | 2.7 | 9.55 | 0.6 | 6.1 | 3.0 |
| A0133 | 3.83 | 0.5 | 2.0 | 0.0 | 15 | 0.1 | 1.9 | 0.0 |
| A0262 | 2.39 | 1.0 | 2.3 | 0.0 | 5.63 | 0.7 | 3.8 | 0.0 |
| A0400 | 59.23 | 0.4 | 22.5 | 52.9 | 95.1 | 0.3 | 24.5 | 61.4 |
| A0478 | 1.57 | 1.9 | 3.0 | 0.0 | 6.9 | 0.4 | 2.6 | 0.0 |
| A0496 | 2.74 | 2.1 | 5.7 | 2.3 | 14.66 | 0.6 | 9.0 | 5.4 |
| A0548e | 12.8 | 0.2 | 2.7 | 0.1 | 17.91 | 0.2 | 2.7 | 0.1 |
| A0576 | 5.25 | 0.6 | 2.9 | 0.3 | 15.01 | 0.2 | 3.1 | 0.1 |
| A0754 | 3.8 | 1.5 | 5.6 | 2.3 | 19.61 | 0.4 | 7.1 | 2.8 |
| A1060 | 2.63 | 1.7 | 4.5 | 0.4 | 13.74 | 0.6 | 7.7 | 0.1 |
| A1367 | 3.68 | 1.8 | 6.4 | 5.6 | 18.64 | 0.4 | 7.7 | 5.0 |
| A1644 | 2.77 | 1.2 | 3.3 | 0.0 | 7.67 | 0.5 | 4.1 | 0.0 |
| A1795 | 0.58 | 2.3 | 1.3 | 0.0 | 5.03 | 0.3 | 1.6 | 0.0 |
| A2065 | 4.99 | 0.8 | 4.2 | 1.5 | 26.23 | 0.2 | 4.5 | 1.5 |
| A2142 | 0.57 | 3.0 | 1.7 | 0.0 | 2.61 | 0.8 | 2.1 | 0.0 |
| A2199 | 1.84 | 2.4 | 4.4 | 1.9 | 7.09 | 0.7 | 4.9 | 1.2 |
| A2244 | 2.23 | 0.6 | 1.4 | 0.0 | 6.86 | 0.2 | 1.4 | 0.0 |
| A2255 | 5.67 | 0.8 | 4.5 | 5.1 | 11.27 | 0.4 | 4.5 | 4.4 |
| A2256 | 0.49 | 2.4 | 1.2 | 0.0 | 2.13 | 0.7 | 1.6 | 0.0 |
| A2589 | 5.06 | 0.5 | 2.7 | 0.0 | 21.48 | 0.2 | 3.8 | 0.0 |
| A2597 | 1.97 | 0.5 | 1.0 | 0.0 | 12.69 | 0.1 | 1.1 | 0.0 |
| A2634 | 6.84 | 0.6 | 3.8 | 0.4 | 15.34 | 0.3 | 4.2 | 0.3 |
| A2657 | 3.01 | 0.7 | 2.1 | 0.0 | 27.51 | 0.2 | 4.1 | 0.1 |
| A2734 | 3.18 | 0.4 | 1.2 | 0.0 | 7.4 | 0.2 | 1.3 | 0.0 |
| A2877 | 2.14 | 0.4 | 0.9 | 0.0 | 16.41 | 0.1 | 1.2 | 0.0 |
| A3112 | 7.57 | 0.8 | 6.0 | 13.8 | 29.98 | 0.2 | 6.1 | 13.4 |
| A3158 | 1.51 | 1.1 | 1.6 | 0.0 | 3.78 | 0.5 | 1.7 | 0.0 |
| A3266 | 1.34 | 2.9 | 3.9 | 2.1 | 6.17 | 0.7 | 4.6 | 1.7 |
| A3376 | 8.43 | 0.6 | 5.4 | 0.5 | 28.36 | 0.3 | 7.5 | 1.2 |
| A3822 | 5.27 | 0.4 | 2.1 | 0.0 | 9.07 | 0.2 | 2.2 | 0.0 |
| A3827 | 0.72 | 0.9 | 0.6 | 0.0 | 3.91 | 0.2 | 0.7 | 0.0 |
| A3921 | 5.96 | 0.4 | 2.5 | 0.6 | 19.58 | 0.1 | 2.7 | 0.6 |
| A4038 | 2.49 | 1.0 | 2.4 | 0.1 | 11.23 | 0.3 | 3.6 | 0.5 |
| A4059 | 2.66 | 0.7 | 2.0 | 0.1 | 11.15 | 0.2 | 2.1 | 0.0 |
| COMA | 0.41 | 10.4 | 4.3 | 0.9 | 1.37 | 4.9 | 6.8 | 2.2 |
| EXO0422 | 0.92 | 0.6 | 0.5 | 0.0 | 4.83 | 0.1 | 0.6 | 0.0 |
| FORNAX | 7.19 | 0.7 | 4.7 | 0.5 | 74.75 | 0.2 | 12.3 | 1.8 |
| HCG94 | 8.44 | 0.3 | 2.6 | 0.0 | 23.26 | 0.2 | 3.7 | 0.0 |
| HYDRA-A | 3.68 | 1.2 | 4.2 | 3.0 | 18.86 | 0.2 | 3.9 | 1.2 |
| II Zw 54 | 12.94 | 0.4 | 4.9 | 0.4 | 52.7 | 0.1 | 4.2 | 0.0 |
| IIZw108 | 3.66 | 0.4 | 1.3 | 0.0 | 6.43 | 0.2 | 1.4 | 0.0 |
| NGC 1550 | 5.38 | 0.5 | 2.5 | 0.0 | 25.85 | 0.2 | 4.9 | 0.0 |
| NGC 5044 | 9.95 | 0.3 | 3.1 | 0.0 | 61.79 | 0.1 | 6.1 | 0.1 |
| RXJ2344 | 5.79 | 0.5 | 2.9 | 1.3 | 30.83 | 0.1 | 2.8 | 0.4 |
| S405 | 3.5 | 0.4 | 1.3 | 0.0 | 6.16 | 0.2 | 1.5 | 0.0 |
| S540 | 14.76 | 0.3 | 4.1 | 1.2 | 48.07 | 0.1 | 4.5 | 1.0 |
| UGC03957 | 10.74 | 0.4 | 4.1 | 0.5 | 75.34 | 0.1 | 5.3 | 0.6 |
| ZwCl1742 | 2.34 | 1.0 | 2.3 | 0.0 | 12.66 | 0.2 | 3.0 | 0.0 |

Notes. Individual flux predictions and upper limits for alternative CR profiles for photon energies above 500 MeV. Columns 2–5 refer to the individual scale factor, the flux prediction above 500 MeV ($F_{\gamma,\text{exp}}^{\text{CR}}$), the derived upper limit on the γ -ray flux, and the individual TS value for the ICM model, while Columns 6–9 represent the values obtained for the flat CR model. All photon fluxes are given in 10^{-10} photon $\text{s}^{-1} \text{cm}^{-2}$.

field of $B \sim 1 \mu\text{G}$ and CR spectral indices $\alpha = 2.1$ – 2.4 , this approach allows the CR energy to be constrained to a few percent while the limits are less stringent for steeper spectra and lower magnetic fields (Aharonian et al. 2009a).

5.6. Hadronic Injection Efficiency

The distributions of CRs within the virial regions of clusters are built up from shocks during the cluster assembly (Ryu et al. 2003; Pfrommer et al. 2006; Pinzke et al. 2013). While strong shocks are responsible for the high-energy population of CRs that could potentially be visible at TeV γ -ray energies, intermediate Mach-number shocks with $\mathcal{M} \simeq 3$ – 4 build up the CR population at GeV energies (Pinzke & Pfrommer 2010), which can be constrained through *Fermi* observations. The normalization of both the CR population and the γ -ray flux scale with the acceleration efficiency at shocks of corresponding strength. Our fiducial CR model (Pinzke & Pfrommer 2010) uses a simplified model for CR acceleration (Enßlin et al. 2007) in which the efficiency rises steeply with Mach number for weak shocks and saturates already at shock Mach numbers $\mathcal{M} \gtrsim 3$. Observations of supernova remnants (Helder et al. 2009) and theoretical studies (Jones & Kang 2005) suggest a value for the saturated acceleration efficiency of $\zeta_{\text{p,max}} \simeq 0.5$, i.e., the fraction of shock-dissipated energy that is deposited in CR ions. Following these optimistic predictions, the model of Pinzke & Pfrommer (2010) assumes this value for the saturated efficiency, which serves as an input to our analysis. This model provides a plausible upper limit for the CR contribution from structure formation shocks in galaxy clusters since more elaborate models of CR acceleration predict even lower efficiencies for the Mach-number range $\mathcal{M} \simeq 3$ – 4 of relevance here (Kang & Ryu 2013, see also Appendix C for a more detailed discussion). If we scale the CR pressure contribution linearly with the maximum acceleration efficiency, using the previously derived limit on A_{γ} , we find $\zeta_{\text{p,max}}^{\text{UL}} = 21\%$ for the combined sample while the CC- and NCC-subsamples yield 25% and 24% maximum acceleration efficiency, respectively. We note that this constrains the maximum acceleration efficiency *only* in the simplified model adopted here. For different acceleration models, these upper limits provide conservative constraints on the acceleration efficiency at intermediate strength shocks of Mach number $\mathcal{M} \simeq 3$ – 4 , a regime complementary to that studied at supernova remnant shocks.

However, these conclusions rely on two major assumptions, namely, CR universality and the absence of efficient CR transport relative to the plasma rest frame. The latter assumption hypothesizes that CRs are tied to the gas via small-scale tangled magnetic fields, which implies that they are only advectively transported and that we can neglect the CR streaming and diffusive transport relative to the rest frame of the gas. Early work on this topic suggests that such CR transport processes are at work in clusters and cause a flattening of radial CR profiles that can significantly reduce the radio and γ -ray emission at high energies probed by Cherenkov telescopes but remains largely unaffected at lower energies probed by *Fermi* (Wiener et al. 2013). Moreover, different formation histories of clusters cause spatial variations of the CR distribution and hence a deviation from a universal distribution (Pinzke & Pfrommer 2010). To date, there is no consensus about the size of these effects, and more work is needed to fully quantify them.

6. SYSTEMATIC UNCERTAINTIES

6.1. Choice of Fiducials: Binning, Region Size, Free Sources

6.1.1. Binning

While the number of spectral bins is the same for the whole sample (nominally 18 bins), the number of spatial bins varies

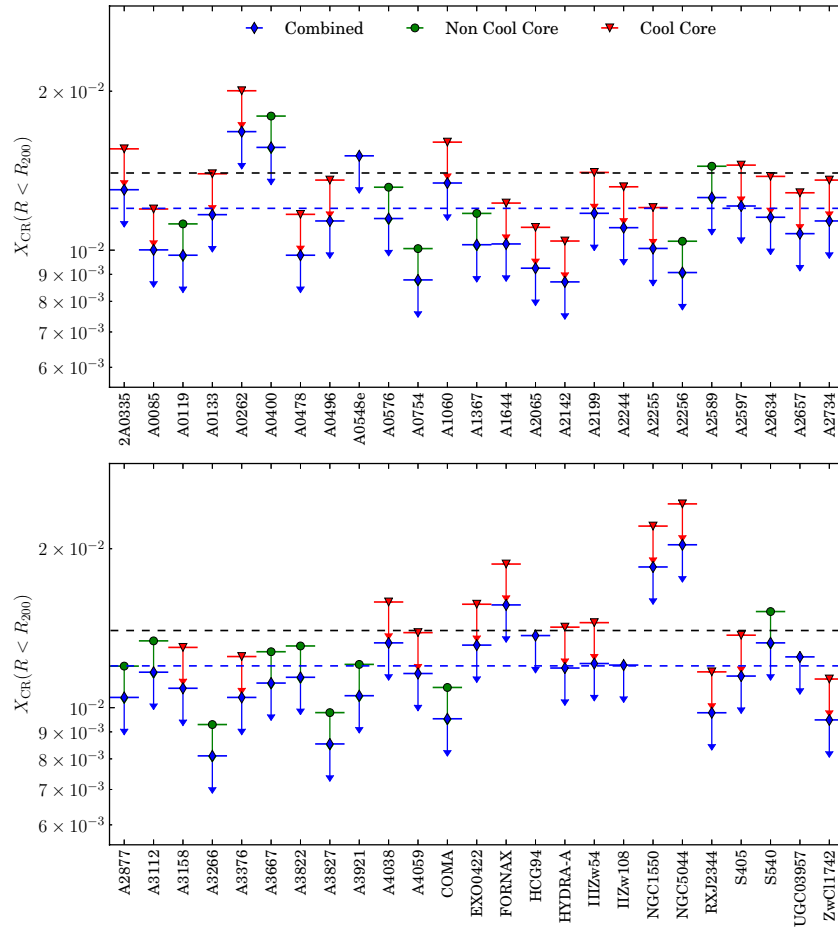


Figure 11. Individual 95% upper limits on X_{CR} for each of our 50 galaxy clusters in this analysis assuming the *jointly derived* scale factor we obtain in our analysis for the full sample (blue diamond), CC clusters (red downward triangle), and NCC clusters (green circle). The dashed lines represent the median upper limit for the combined (blue) while the median upper limits for CC and NCC are the same (shown in black).

(A color version of this figure is available in the online journal.)

with the ROI size, because the bin width is constant (0.1°). In addition, the extended templates used to model the cluster emission are also binned. To check the effect of binning, we vary the nominal values by 50%. Aside from potentially increasing the computation time for larger numbers of spatial bins, we find that our choice of binning does not change the results by more than $\sim 1\%$. Similarly, we find that varying the number of spectral bins changes the resulting limits on A_γ by at most 5%.

6.1.2. Region Size

We use ROIs of varying sizes, ranging from 8° – 16° in radius (Table 2). To make sure that this choice does not introduce any significant bias, we compare the fitted values for all free parameters for the null hypothesis in these smaller regions with ROIs with 25% larger radii and find variations of these values which are less than 3% with respect to larger regions. However, we note that larger regions allow a more stringent determination of the background model which is reflected by smaller uncertainties on the Galactic and isotropic diffuse components than for the case of smaller regions (compare to error bars in Figure 5).

6.1.3. Free Sources

We choose to use the two year source list to model the data collected during four years of LAT observations. While we ensure that residual excesses are mitigated by allowing the

normalizations of the known point sources to vary, the choice of leaving the normalizations of sources within 4° of each cluster to vary freely is somewhat arbitrary. Freeing the normalizations of only those sources within $\theta_{200} + 1^\circ$ does not change our results on A_γ by more than 10%.

6.2. Event Classes and Instrument Response Functions

The IRFs consist of three separate parts (see Ackermann et al. 2012a, for details): the effective area which has an associated uncertainty of at most $\sim 10\%$ in the energy range we consider, the PSF whose uncertainty can be conservatively estimated to be $\sim 15\%$, and the energy dispersion (whose uncertainty is negligible for this analysis). Using bracketing IRFs (see Sections 5.7.1 and 6.5.1 in Ackermann et al. 2012a) to quantify these uncertainties, we find that while individual ROIs may show variations of up to $\sim 21\%$, the effect on the combined scale factors and quantities derived from it is less than 7%.

6.3. Diffuse Emission

Spatial residuals due to mismodeling of the large-scale Galactic diffuse foreground emission may be misinterpreted in terms of an extended γ -ray excess. We compare results derived using the standard diffuse emission model adopted for the baseline analysis (based on empirical fits of multiple spatial templates to γ -ray data) to results obtained when using a set of eight alternative diffuse emission models that were created using

Table 8

Alternative Models for Galactic Diffuse Emission

| Label | CR Source Distribution | Halo Size (kpc) | Spin Temperature (K) |
|-------|------------------------|-----------------|----------------------|
| A | Lorimer | 10 | 10^5 |
| B | Lorimer | 10 | 150 |
| C | Lorimer | 4 | 10^5 |
| D | Lorimer | 4 | 150 |
| E | SNR | 10 | 10^5 |
| F | SNR | 10 | 150 |
| G | SNR | 4 | 10^5 |
| H | SNR | 4 | 150 |

Notes. Overview of the alternative diffuse models used for assessing the systematic uncertainties in the model for the Galactic diffuse emission. We chose to vary the three most important input parameters that were found in scanning the parameter space in Ackermann et al. (2012c).

a different methodology with respect to the standard diffuse emission model.⁷⁴

We chose these models to represent the most important parameters scanned in Ackermann et al. (2012c), in particular, CR source distribution, halo size, and spin temperature. We summarize the properties of the alternative models in Table 8, and we refer readers to de Palma et al. (2013) for details. The models we employed were tuned to the P7REP data. Although the models were created such that different components along the l.o.s. could be fit separately, we only adopted a free overall normalization, since at high Galactic latitudes the vast majority of the gas resides in the neighborhood of the solar system. Moreover, having different components as additional degrees of freedom in the fit makes a comparison of the TS values with the baseline analysis more difficult.

We emphasize that these eight models do not span the complete uncertainty of the systematics involved with interstellar emission modeling. They do not even encompass the full uncertainty in the input parameters that are varied. The resulting uncertainty should therefore only be considered as one indicator of the systematic uncertainty due to interstellar emission modeling. The tests we performed using these additional models considered a different energy range, from 500 MeV–100 GeV, because the alternative models were not derived for higher energies. However, since events at low energies dominate the fit, this difference is negligible. We have explicitly verified this by repeating the baseline analysis up to 100 GeV and we found that the differences between the computed combined scale factors are $<1\%$.

In Figure 12, we show how the combined upper limit on the scale factor, A_γ^{UL} , varies for the alternative models with respect to our standard model as well as how the significance of the excesses observed in A1367 and A3112, and A400 changes when using the alternative models.

The spread in limits for the scale factor is rather small between the alternative diffuse models, but the choice of using the standard diffuse model versus any of the alternative diffuse models can affect the inferred limits for the different cluster samples by 20%–30%. Comparing the TS values for the three clusters indicates small variations across the alternative models for A400, A3112, and A1367. We repeated this procedure for the derivation of the individual flux limits (see Section 5.4) and found that the majority of our clusters follow the same trend. We

⁷⁴ We also use a different set of isotropic diffuse templates that were created in conjunction with the alternative Galactic diffuse templates.

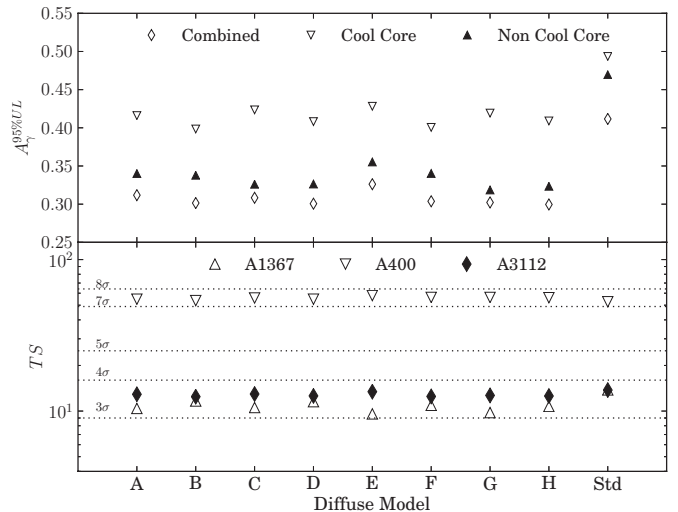


Figure 12. In the upper panel, we show the 95% combined upper limit on A_γ for the respective (sub)samples for the alternative diffuse models (A–H, see Table 8 and the accompanying text for details). In the bottom panel, we show the associated TS values for the three clusters that exhibit significant excess emission.

have marked the clusters which show variations beyond 30% in Table 6.

We summarize the systematic uncertainties discussed in this section in Table 9, and we note that the main source of uncertainty is the accurate modeling of the foreground Galactic diffuse emission.

7. SUMMARY AND CONCLUSIONS

We have used a data set of 4 yr of all-sky data from the *Fermi*-LAT detector and performed a search for high-energy γ -ray emission originating from 50 X-ray luminous galaxy clusters. We specifically consider hadronically induced γ rays originating from the ICM as described by the universal CR model by Pinzke & Pfrommer (2010) and employ a joint likelihood analysis to constrain the normalization of a common scale factor among clusters that is theoretically expected to describe the γ -ray luminosity of the ICM. In order to allow for different emission scenarios, we categorize clusters in our sample by their morphologies and separately consider CC and NCC subsamples.

We find evidence for excess emission at a significance of 2.7σ , naively taken as a first indication of γ -ray emission from galaxy clusters. However, upon closer investigation, we find that this global significance originates mainly from individual excesses present in three galaxy clusters: A1367, A3112, and A400, the latter yielding a post-trial significance of 6.7σ alone. For these three clusters, the LAT data alone cannot conclusively support or reject the hypothesis that the excess emission arises from within the clusters. The best-fit location of each excess is located within the virial radius of the respective cluster, but it is offset from the cluster center.

With respect to the universal CR model, we also note that the associated scale factors are significantly larger than the ones derived from other clusters in the sample. We also argue that in all three clusters there are individual radio galaxies which may be the origin of observed excesses.

We establish bounds on the common scale factor A_γ , and we use this to derive individual upper limits on the γ -ray flux. In addition, we use the jointly derived limit on A_γ to calculate

Table 9
Systematic Uncertainties

| Type | Variation of Input Parameters | Impact on Results |
|-----------------------------------|---|-------------------------------|
| Spectral bins | $\pm 50\%$ | $< 5\%$ |
| Spatial bins | $\pm 50\%$ | $< 1\%$ |
| Spatial template bins | $\pm 50\%$ | $< 1\%$ |
| Small ROIs | $+25\%$ | $\sim 3\%$ |
| Number of free sources | $4^\circ \rightarrow \theta_{200} + 1^\circ$ ^a | $< 10\%$ |
| IRF uncertainties: effective area | $\pm 10\%$ ^b | $< 7\%$ |
| IRF uncertainties: PSF | $\pm 15\%$ ^b | $< 4\%$ |
| Diffuse model uncertainties | Alternative diffuse models ^c | 15%–25% more stringent limits |

Notes. Overview of systematic uncertainties as discussed in Section 6. We note that the largest impact on the results is due to the model for the Galactic diffuse emission.

^a We chose a radius of 4° around each cluster center to account for photon contamination due to the PSF at low energies. In this test, we modify the radius in which we leave the normalization free to vary within $\theta_{200} + 1^\circ$.

^b We employ the *bracketing IRF* approach as discussed in Ackermann et al. (2012a) and use the tabulated values to scale the relevant IRF components.

^c We use a set of alternative diffuse emission models and replace the standard emission template used in the baseline analysis with these.

limits on the volume-averaged CR-to-thermal pressure $\langle X_{\text{CR}} \rangle$. We compute median upper limits calculated within R_{200} , with the most stringent one being $\langle X_{\text{CR}} \rangle < 0.012$ for the combined sample and $\langle X_{\text{CR}} \rangle < 0.013$ and $\langle X_{\text{CR}} \rangle < 0.014$ for the CC and NCC sub-samples, respectively. Assuming a linear dependence, our limits on A_γ translate into a combined limit of the hadronic injection efficiency, $\zeta_{\text{p,inj}}$, by large-scale structure formation shocks in the Mach number range $\mathcal{M} \simeq 3\text{--}4$ to be below 21% for the combined sample and 25% and 24% for the CC and NCC clusters, respectively. Removing the aforementioned three clusters that exhibit excess emission provides even more stringent limits on A_γ , which for the combined sample, yields $A_\gamma^{\text{UL}} = 0.29$ that translates into $\langle X_{\text{CR}} \rangle < 0.008$ within R_{200} and $\zeta_{\text{p,inj}}(\mathcal{M} \simeq 3\text{--}4) < 15\%$. Our limits on $\langle X_{\text{CR}} \rangle$ and $\zeta_{\text{p,inj}}$ are the most stringent to date, constraining hadronic emission scenarios that predict astrophysical γ rays originating in the ICM of galaxy clusters.⁷⁵

The systematic uncertainty associated with the modeling of the Galactic foreground emission represents the largest source of uncertainty affecting limits on extended emission from the ICM presented in this work. To account for this, we have tested our results against a set of alternative diffuse models spanning a range of interstellar emission model parameters. We find that the alternative models provide limits that differ from the baseline analysis by 20%–30%.

We thank the referee for a thoughtful report that helped improve the paper. The *Fermi*-LAT Collaboration acknowledges generous ongoing support from a number of agencies and institutes that have supported both the development and the operation of the LAT as well as scientific data analysis. These include the National Aeronautics and Space Administration and the Department of Energy in the United States; the Commissariat à l’Énergie Atomique and the Centre National de la Recherche Scientifique/Institut National de Physique Nucléaire et de Physique des Particules in France; the Agenzia Spaziale Italiana and the Istituto Nazionale di Fisica Nucleare in Italy; the Ministry of Education, Culture, Sports, Science and Technology (MEXT), High Energy Accelerator Research Organization (KEK), and Japan Aerospace Exploration Agency (JAXA)

in Japan; and the K. A. Wallenberg Foundation, the Swedish Research Council, and the Swedish National Space Board in Sweden. Additional support for science analysis during the operations phase is gratefully acknowledged from the Istituto Nazionale di Astrofisica in Italy and the Centre National d’Études Spatiales in France. J.C. is a Wallenberg Academy Fellow. C.P. gratefully acknowledges financial support of the Klaus Tschira Foundation. AP acknowledges the NASA grant NNX12AG73G for support. We thank our referee for the useful comments that improved the quality of this paper. This research has made use of the NASA/IPAC Extragalactic Database (NED) which is operated by the Jet Propulsion Laboratory, California Institute of Technology, under contract with the National Aeronautics and Space Administration.

Facility: Fermi

APPENDIX A

MC SIMULATION STUDIES

We use the simulation package *gtobssim* to efficiently generate MC realizations of the γ -ray sky using the parametrized instrument response.

A.1. Minimum Energy Threshold

The joint likelihood approach discussed in Section 3.1 makes the assumption that the individual data samples are uncorrelated. Assuming two sources s_1 and s_2 , in the uncorrelated case, the composite p -value is $p_\Sigma = p_1 \times p_2$, where p_1 and p_2 are the p -values associated with s_1 and s_2 , respectively. This case corresponds to two sources that are far away from each other. In this case, the difference between p_{joint} , which is the derived p -values from the joint likelihood, should be minimal, while for small distances, correlations impact the derivation of p_{joint} , and thus lead to an overestimation of the significance associated with this p -value. We assess this bias using an isotropic simulation with two identical power-law sources with $\Gamma = -2.3$ that were each modeled as an extended source with a disk of 2° in diameter. In Figure 13, we show the difference between p_{joint} and p_Σ . We find that at small distances ($< 3^\circ$), for all minimum energy thresholds, there is a substantial bias due to overlaps. Toward larger distances, this bias is reduced. In this toy model, 3° corresponds to $R_{200} + 1^\circ$. However, by requiring

⁷⁵ Note that all these limits are computed at the 95% C.L.

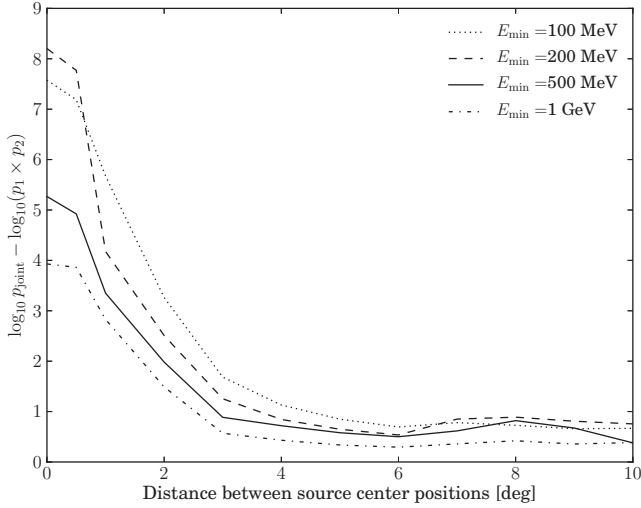


Figure 13. We show the difference between the jointly derived p -value and the case of uncorrelated samples, where $p_{\Sigma} = p_1 \times p_2$ (see text for details) simulating two power-law sources with identical spectral model and modeled as a disk with 2° in diameter for a minimum energy threshold E_{\min} of (100 MeV, 200 MeV, 500 MeV, and 1 GeV). The solid line corresponds to our analysis threshold, chosen to minimize this overlap bias while maximizing the expected γ -ray flux.

larger distances between sources, we reduce the number of viable cluster candidates for our search. Hence we decided to use $E_{\min} = 500$ MeV as this threshold maximizes the number of clusters to be included (and thus the expected signal) while minimizing the bias on p_{joint} .

A.2. Significance Assessment

In Figure 14, we show ROI-specific TS-distributions for a background only simulation (top). We find that the TS-distribution in the background-only case can be well described by $(1/2)\delta + (1/2)\chi_k^2$ and obtain $k = 1.1 \pm 0.1$ in an unbinned maximum likelihood fit, giving rise to the usual definition of significance as $\sqrt{\text{TS}}$.

A.3. Signal Studies

In addition, we include the results from simulations including a (weak) putative CR-induced γ -ray signal corresponding to $A_{\gamma} = 0.29$ (nominal best-fit value for the combined sample) as well as $A_{\gamma} = 1$ (middle panel in Figure 14), i.e., assuming the predictions by Pinzke et al. (2011). Finally, we repeat the analysis assuming a strong signal, characterized by $A_{\gamma} = 10$ (bottom panel in Figure 14). For all simulations, the true value of A_{γ} is recovered in the combined result, validating our analysis

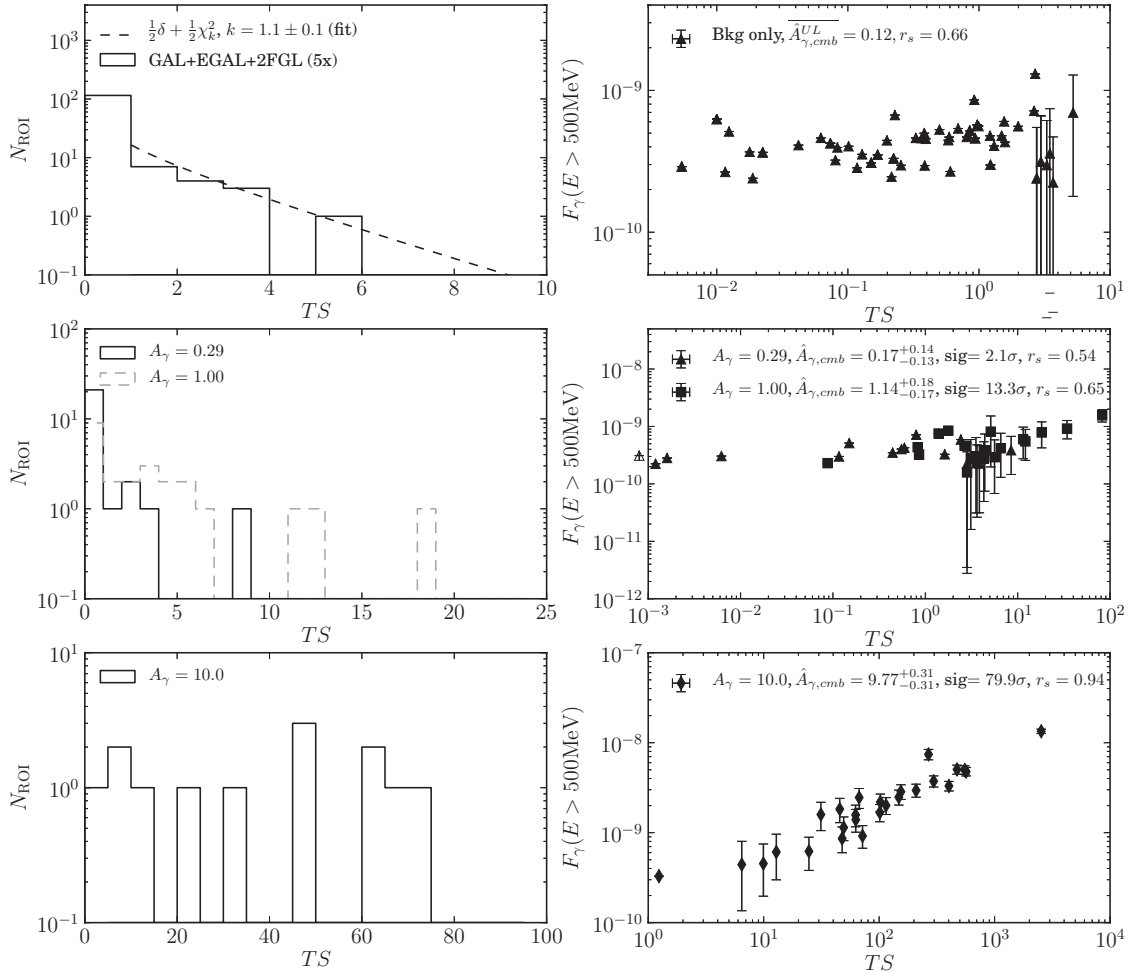


Figure 14. In the top left panel, we show the TS-distribution for five background-only simulations and fit the distribution to the null hypothesis according to our analysis (refer to Section 3.1 for details). In the top right panel, we show the constraints on the γ -ray flux using the ROI-specific individual scale factors $A_{\gamma,i}$ and relate them to the associated TS values. r_s denotes the Spearman rank correlation coefficient and sig refers to the combined significance derived from $\text{TS}_{\text{global}}$. The middle and lower panel show the same but assume a putative γ -ray source in addition to the background. We show that for $A_{\gamma} = 1$ and even more so for $A_{\gamma} = 10$ the TS-distributions clearly depart from a χ^2 distribution. It should be noted, however, that while the background simulation is based on five MC realizations of the γ -ray sky, the various signal simulations represent a single example realization for each assumed signal.

approach, although the global significance varies with respect to the signal simulation. For the background-only case, only upper limits can be derived. Assuming the nominal best-fit value for A_γ from the combined sample, yields a combined significance of 2.1σ . For $A_\gamma = 1$ and $A_\gamma = 10$, these values are much higher, yielding a global TS value corresponding to a significance of 13.3σ and 79.9σ , respectively.

Given that a simulation with $A_\gamma = 0.29$ yields a combined significance comparable with what we have found in our analysis, we investigated how this signal could be studied further. To that end, we compare the expected γ -ray flux based on the ROI-specific scale factors $A_{\gamma,i}$ with their associated ROI TS values and quantify the correlation through calculating Spearman-rank correlation coefficient (Spearman 1904), denoted by r_s . We find Spearman-rank coefficients >0.5 indicating a correlation. However, even for the background case, $r_s = 0.6$ is obtained, which is the same as what we find in the signal case for $A_\gamma = 1$. This illustrates that a correlation analysis with such a weak signal, or further, studying the excess we find, is difficult. Only for the strong signal of $A_\gamma = 10$ do we find a correlation coefficient $r_s = 0.94$ indicating a strong correlation between expected γ -ray flux and associated ROI TS value.

APPENDIX B

ANALYTIC COSMIC-RAY MODEL

Following the analytic CR formalism (Pfrommer & Enßlin 2004a; Pfrommer et al. 2008; Pinzke & Pfrommer 2010), we obtain the volume-weighted, energy-integrated, and omnidirectional (i.e., integrated over the 4π solid angle) γ -ray source function due to pion decay,

$$\lambda_{\pi^0-\gamma}(R, E) = \kappa_{\pi^0-\gamma}(R) \lambda_{\pi^0-\gamma}(> E). \quad (\text{B1})$$

Here the spatial part of the γ -ray emission is determined by

$$\kappa_{\pi^0-\gamma}(R) = C_{\text{CR}}(R) \rho_{\text{gas}}(R), \quad (\text{B2})$$

where the CR proton distribution is

$$\frac{\tilde{C}_{\text{CR}}(R)}{\rho_{\text{gas}}(R)} = (C_{200} - C_{\text{center}}) \left(1 + \left(\frac{R}{R_{\text{trans}}} \right)^{-\beta} \right)^{-1} + C_{\text{center}}, \quad \text{and} \quad (\text{B3})$$

$$C_{200} = 1.7 \times 10^{-7} \times (M_{200}/10^{15} M_\odot)^{0.51}, \quad (\text{B4})$$

$$R_{\text{trans}} = 0.021 R_{200} \times (M_{200}/10^{15} M_\odot)^{0.39}, \quad (\text{B5})$$

$$\beta = 1.04 \times (M_{200}/10^{15} M_\odot)^{0.15}, \quad (\text{B6})$$

where $\tilde{C} = Cm_p/\rho$ denotes the dimensionless normalization of the CR distribution function. For massive clusters ($M_{200} \sim 10^{15} M_\odot$) the CR distribution traces the gas density, while the CR density is slightly enhanced in the center for smaller systems. Note, however, that the γ -ray flux depends only weakly on the exact CR density in the center (i.e., C_{center}) since most of the flux originates from outside the transition region.

The spectral part of Equation (B1) for the photon energies relevant to *Fermi*-LAT ($100 \text{ MeV} \lesssim E_\gamma \lesssim 1 \text{ TeV}$) is given by

$$\begin{aligned} \lambda_{\pi^0-\gamma}(> E) &= \frac{4m_{\pi^0}c}{3m_p^3} \times \sum_{i=1}^3 \frac{\sigma_{\text{pp},i}}{\alpha_i \delta_i} \left(\frac{m_p}{2m_{\pi^0}} \right)^{\alpha_i} \\ &\times \Delta_i \left[\mathcal{B}_x \left(\frac{\alpha_i + 1}{2\delta_i}, \frac{\alpha_i - 1}{2\delta_i} \right) \right]_{x_1}^{x_2}, \\ \text{and } x_j &= \left[1 + \left(\frac{m_{\pi^0}c^2}{2E_{\gamma,j}} \right)^{2\delta_i} \right]^{-1}, \quad (\text{B7}) \end{aligned}$$

where the sum over i extends over $\Delta = (0.767, 0.143, 0.0975)$, and $\alpha = (2.55, 2.3, 2.15)$. The γ -ray spectrum rises until a maximum at the mass of the π^0 meson followed by a concave shaped tail determined by the universal CR spectrum. The shape parameter $\delta_i \simeq 0.14 \alpha_i^{-1.6} + 0.44$ allows us to accurately predict the emission close to the pion bump in combination with the effective inelastic cross-section for proton-proton interactions, $\sigma_{\text{pp},i} \simeq 32 (0.96 + e^{4.42-2.4\alpha_i})$ mbarn. We have also introduced the equation

$$[\mathcal{B}_x(a, b)]_{x_1}^{x_2} = \mathcal{B}_{x_2}(a, b) - \mathcal{B}_{x_1}(a, b), \quad (\text{B8})$$

where $\mathcal{B}_x(a, b)$ denotes the incomplete Beta-function.

APPENDIX C

RELATIONSHIP BETWEEN CR ACCELERATION EFFICIENCY AND GAMMA-RAY FLUX

In this Appendix, we investigate how we can use upper limits on the γ -ray flux to constrain the CR injection efficiency in various models for CR acceleration. The CR model adopted in this paper (Pinzke & Pfrommer 2010) is based on a simplified scheme (Enßlin et al. 2007) to compute the CR-energy acceleration efficiency at shocks (in units of the shock-dissipated thermal energy, corrected for adiabatic compression), $\zeta_{\text{p},\text{inj}}(\mathcal{M}) = \varepsilon_{\text{CR}}/\varepsilon_{\text{diss}}$. It employs the thermal leakage model (e.g., Ellison & Eichler 1984; Berezhko et al. 1994; Kang & Jones 1995), which conjectures a momentum threshold for injection that is a constant multiple ($x_{\text{inj}} = 3.5$) of the peak thermal momentum, at which the CR power-law distribution connects to the post-shock Maxwellian. More refined models (such as in Kang & Ryu 2011, 2013) are motivated by nonlinear shock acceleration, and they fix the injection momentum by the considering that the particle speed should be several times larger than the downstream flow speed in order for suprathermal particles to diffuse upstream across the shock transition layer. This yields a Mach-number dependent x_{inj} , which increases for weaker shocks such that a progressively smaller fraction of particles can participate in the process of diffusive shock acceleration. As a result, for the preferred values of the ratio of the downstream turbulent-to-background field, $\varepsilon_B \gtrsim 0.25$, those models predict $\zeta_{\text{p},\text{max}} \gtrsim 0.4\text{--}0.5$, depending on the existence of a pre-existing CR population.⁷⁶ While those values for the acceleration efficiency are now challenged by γ -ray observations of supernova remnants, additional physics (such as amplification mechanisms of the magnetic field) may lower the value of ε_B and cause the acceleration efficiency to saturate at lower values (Kang & Ryu 2013).

⁷⁶ This is obtained by taking the ratio of CR acceleration efficiency (η) and gas thermalization efficiency (δ) in the limit of large Mach numbers (Kang & Ryu 2013).

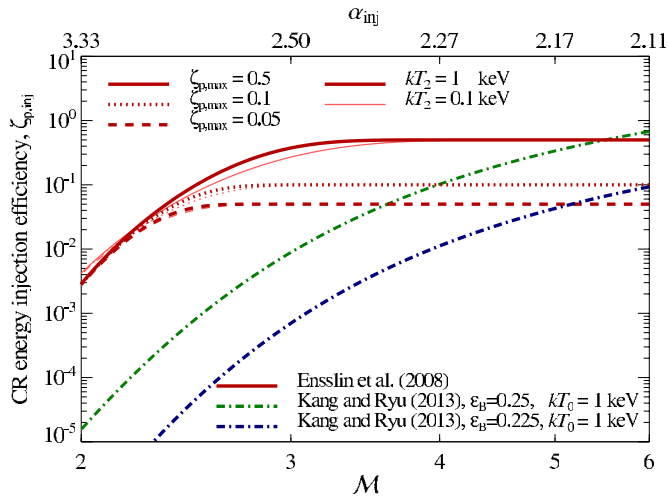


Figure 15. Acceleration efficiency $\zeta_{p,inj}$ as a function of shock Mach number (\mathcal{M}) for two different post-shock temperatures of 0.1 keV (thick bright) and 1 keV (thin faded). We show the acceleration efficiency that was used in our simulations ($\zeta_{p,max} = 0.5$, red solid) and that was scaled to different values for the saturated acceleration efficiency ($\zeta_{p,max} = 0.1$ and $\zeta_{p,max} = 0.05$; red dotted and dashed, respectively). Also shown in blue and green is the acceleration efficiency in a model by Kang & Ryu (2013) for different values of ϵ_B , the ratio of downstream turbulent-to-background magnetic field, which determines the injection efficiency in their model. Since shocks with Mach numbers $\mathcal{M} \simeq 3-4$ are mostly responsible for injecting CRs in clusters, constraints on $\zeta_{p,inj}$ in the model by Enßlin et al. (2007) are more conservative in comparison to the model by Kang & Ryu (2013).

(A color version of this figure is available in the online journal.)

Moreover, in weak heliospheric shocks, additional shock phenomena (e.g., whistler waves in the shock front, etc.) are observed that may add to the uncertainty of the acceleration efficiency. In summary, while the models for the acceleration efficiency in shocks became more detailed and physical over the last year, new observations point to the necessity of further improving those models.

In Figure 15, we show the relation between acceleration efficiency and shock Mach number. For the relevant energy regime that we consider in this work ($E_\gamma \gtrsim 500$ MeV), our CR model predicts a CR spectral index of $\simeq 2.4$ that flattens toward higher energies (Pinzke & Pfrommer 2010). This implies that shocks with Mach numbers $\mathcal{M} \gtrsim 3.5$ (depending somewhat on the post-shock temperature) are the most relevant for the CR budget. Because the acceleration efficiency has already saturated for this range of shock strengths in the model of Enßlin et al. (2007), the CR pressure and thus the hadronically induced γ -ray luminosity are approximately proportional to $\zeta_{p,max}$. For different acceleration models (such as in Kang & Ryu 2013), these upper limits provide interesting constraints on the acceleration efficiency at intermediate strength shocks of Mach number $\mathcal{M} \simeq 3-4$, a regime complementary to that studied at supernova remnant shocks.

APPENDIX D

RADIO AND X-RAY SOURCES IN THE FIELD OF VIEW OF A3112, A1367 AND A400

In this section, we provide a discussion of the radio sources in the field of view of the three clusters as discussed in Section 5.3. We note that a detailed characterization of the origin of the excess emission is beyond the scope of this work. Based on the refined best-fit positions from our higher resolution TS-map, we performed a search for sources within the 3σ contours as shown in Figure 16. Below, we provide supplemental information regarding the three clusters discussed in the main text.

1. For A1367, our best-fit position is consistent with that of the radio galaxy 3C264 (Fey et al. 2004). As we cannot distinguish between A1367 and 3C264, we conclude by similarity with previous γ -ray detections in clusters that we likely observe γ -ray emission from the radio galaxy (e.g., M87 in Virgo or IC 310 in Perseus).
2. Similarly, the origin of the emission toward A3112 may be from the radio galaxy PKS 0316-444, which is located

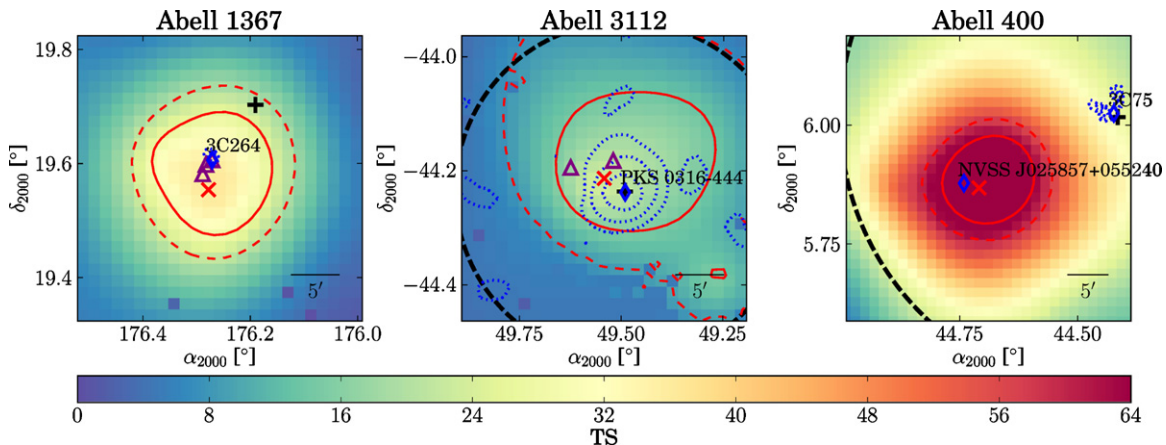


Figure 16. TS maps of our three cluster candidates with $TS > 9$. Each map shows a $0.5^\circ \times 0.5^\circ$ section ($0.6^\circ \times 0.6^\circ$ for A400) that was recentered to the best-fit position obtained using `gtfindsrc`. The best-fit position from the refined TS calculations is marked as red \times . Shown in red are the 3σ (solid) and 4σ contours (dashed). The blue diamond-shaped points correspond to the NED positions of the radio galaxies as discussed in the text. The purple upright open triangles denote Chandra X-ray sources that fall within the error circle of the γ -ray point source. Overlaid radio contours (blue dotted) were obtained from the NVSS for A1367 and A400 (Condon et al. 1998). The radio contours for A3112 were obtained from the Parkes-MIT-NRAO Survey (Condon et al. 1994). The cluster center is marked by a black cross in each panel. The virial radius of the cluster is indicated by the dashed black line (partially visible in the maps for both A3112 and A400). Coordinates are taken from NED/SIMBAD. Each pixel is 0.2 across.

(A color version of this figure is available in the online journal.)

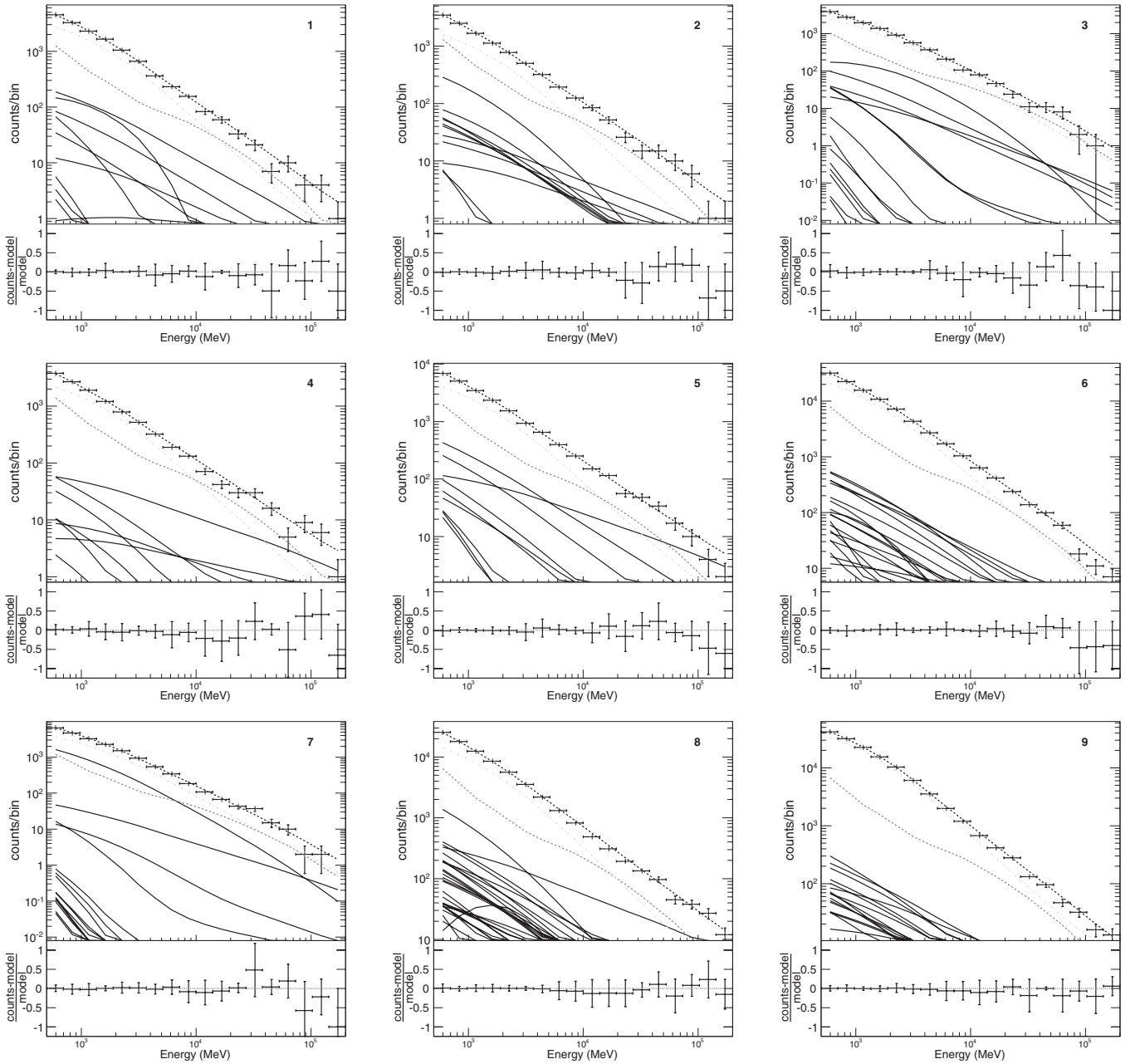


Figure 17. Fitted counts spectra for 9 of the 26 analysis ROIs without additional cluster sources. The crosses indicate the measured counts in each energy bin while the black dashed lines show the total sum of all model counts for all components. The gray dashed lines refer to the Galactic diffuse component while the gray dotted lines correspond to the isotropic extragalactic diffuse component. Solid lines indicate additional background sources. We obtain reasonable fits in all energy bins. The lower panel for each ROI shows fractional residual counts integrated over the entire ROI.

4/2 away from the best-fit position of the excess (Costa & Loyola 1998).

3. In the vicinity of the best-fit position of the excess toward A400, a (not further classified) radio source NVSS J025857+055240 was reported by Condon et al. (1998). Because of this positional coincidence, it is plausible to attribute the observed γ -ray emission to this object, although this hypothesis warrants further investigation.

In addition to the previously discussed radio sources, there are multiple *Chandra* X-ray sources that fall within the error circle of the best-fit positions for the excesses in A1367 and A3112, respectively. While the association of the excesses in γ rays

with individual radio galaxies is well in line with previous γ -ray detections, e.g., M87 in Virgo or NGC 1275 and IC 310 in Perseus, the similarity argument we present here is not sufficient to claim detection of γ rays from these respective objects.

APPENDIX E

ROI-SPECIFIC COUNTS/MODEL COMPARISON

We provide for each ROI the observed photon counts in each energy bin along with the predicted model counts from the best-fit background-only model and show this in Figures 17–19.

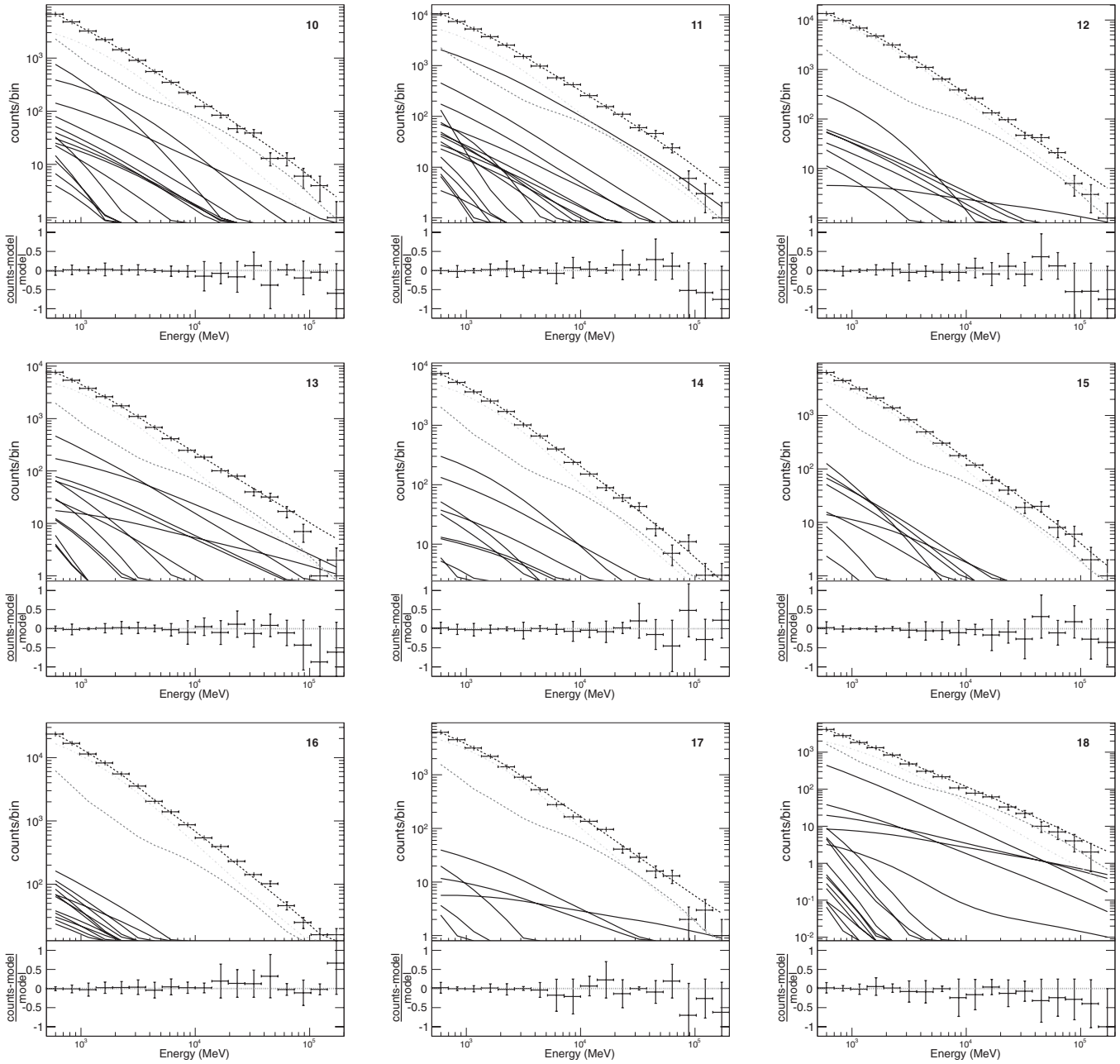


Figure 18. Fitted spectra for ROIs 10-18. See caption of Figure 17 for details.

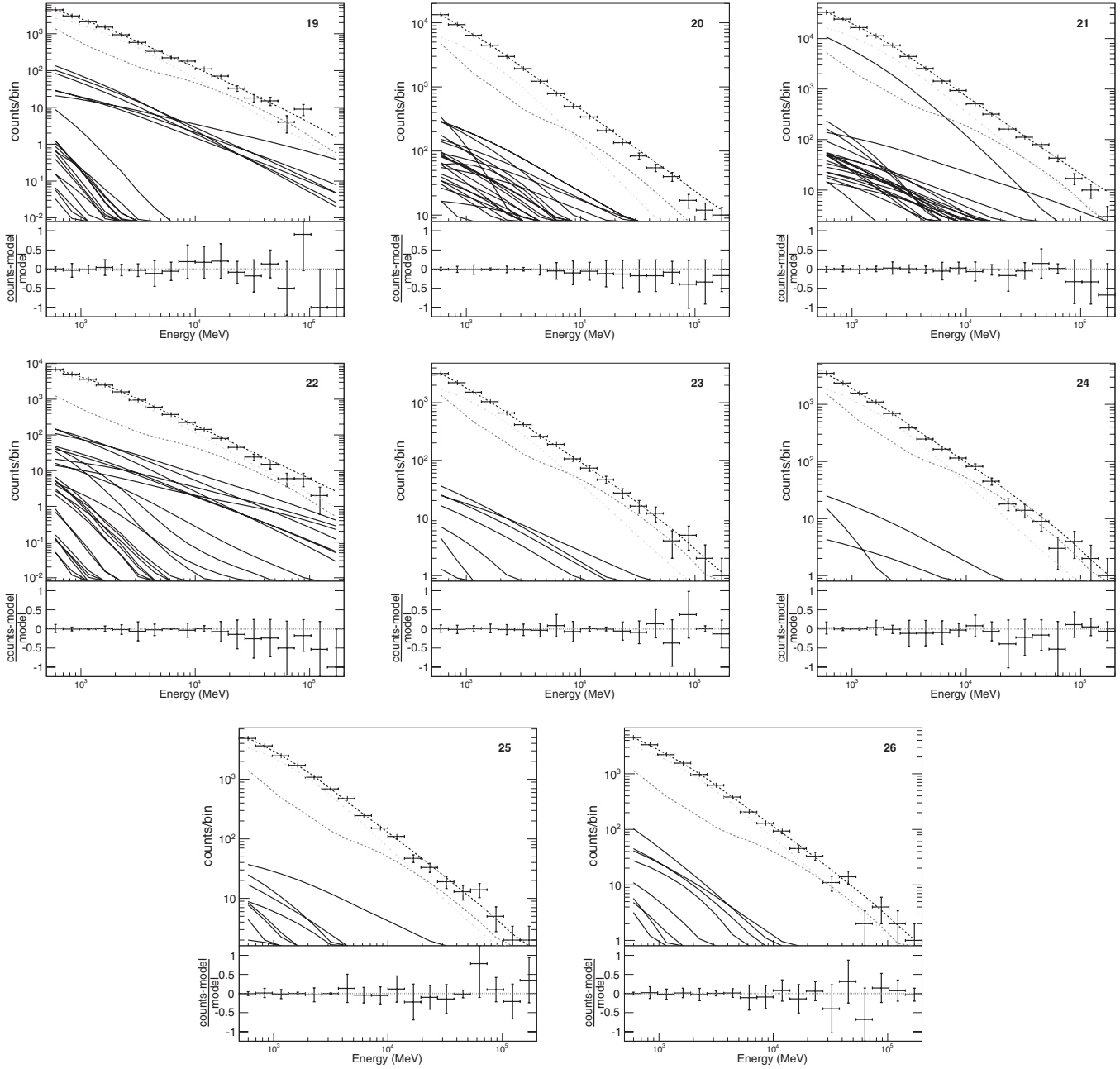


Figure 19. Fitted spectra for ROIs 19-26. See caption of Figure 17 for details.

REFERENCES

- Abdo, A. A., Ackermann, M., Ajello, M., et al. 2009, *ApJ*, 699, 31
- Abramowski, A., Acero, F., Aharonian, F., et al. 2012, *ApJ*, 750, 123
- Ackermann, M., Ajello, M., Albert, A., et al. 2011, *PhRvL*, 107, 241302
- Ackermann, M., Ajello, M., Albert, A., et al. 2012a, *ApJS*, 203, 4
- Ackermann, M., Ajello, M., Allafort, A., et al. 2010a, *JCAP*, 05, 025
- Ackermann, M., Ajello, M., Allafort, A., et al. 2010b, *ApJL*, 717, L71
- Ackermann, M., Ajello, M., Allafort, A., et al. 2012b, *Sci*, 338, 1190
- Ackermann, M., Ajello, M., Atwood, W. B., et al. 2012c, *ApJ*, 750, 3
- Ackermann, M., Albert, A., Anderson, B., et al. 2014, *PhRvD*, 89, 042001
- Aharonian, F., Akhperjanian, A., Beilicke, M., et al. 2003, *A&A*, 403, L1
- Aharonian, F., Akhperjanian, A. G., Anton, G., et al. 2009a, *A&A*, 502, 437
- Aharonian, F., Akhperjanian, A. G., Anton, G., et al. 2009b, *A&A*, 495, 27
- Aleksić, J., Alvarez, E. A., Antonelli, L. A., et al. 2012a, *A&A*, 541, A99
- Aleksić, J., Alvarez, E. A., Antonelli, L. A., et al. 2012b, *A&A*, 539, L2
- Aleksić, J., Antonelli, L. A., Antoranz, P., et al. 2010a, *ApJL*, 723, L207
- Aleksić, J., Antonelli, L. A., Antoranz, P., et al. 2010b, *ApJ*, 710, 634
- Ando, S., & Nagai, D. 2012, *JCAP*, 07, 017
- Arlen, T., Aune, T., Beilicke, M., et al. 2012, *ApJ*, 757, 123
- Atwood, W. B., Abdo, A. A., Ackermann, M., et al. 2009, *ApJ*, 697, 1071
- Bartlett, M. 1953, *Biometrika*, 40, 306
- Bereztko, E. G., Yelshin, V. K., & Ksenofontov, L. T. 1994, *Aph*, 2, 215
- Berezinsky, V. S., Blasi, P., & Ptuskin, V. S. 1997, *ApJ*, 487, 529
- Blasi, P., & Colafrancesco, S. 1999, *Aph*, 12, 169
- Blasi, P., Gabici, S., & Brunetti, G. 2007, *IJMPA*, 22, 681
- Bregeon, J., Charles, E., & Wood, M. for the Fermi-LAT collaboration. 2013, in Proc. 2012 Fermi Symp., eConf Proceedings C121028 (Washington, DC: NASA), arXiv:1304.1395
- Brunetti, G., & Blasi, P. 2005, *MNRAS*, 363, 1173
- Brunetti, G., Blasi, P., Cassano, R., et al. 2004, *MNRAS*, 350, 1174
- Brunetti, G., Blasi, P., Reimer, O., et al. 2012, *MNRAS*, 426, 956
- Brunetti, G., Cassano, R., Dolag, K., et al. 2009, *A&A*, 507, 661
- Brunetti, G., & Lazarian, A. 2007, *MNRAS*, 378, 245
- Brunetti, G., & Lazarian, A. 2011, *MNRAS*, 410, 127
- Brunetti, G., Setti, G., Feretti, L., et al. 2001, *MNRAS*, 320, 365
- Brunetti, G., Venturi, T., Dallacasa, D., et al. 2007, *ApJL*, 670, L5
- Cavagnolo, K. W., Donahue, M., Voit, G. M., et al. 2009, *ApJS*, 182, 12
- Chen, Y., Reiprich, T. H., Böhringer, H., et al. 2007, *A&A*, 466, 805
- Chernoff, H. 1952, *Ann. Math. Stat.*, 23, 493
- Churazov, E., Forman, W., Vikhlinin, A., et al. 2008, *MNRAS*, 388, 1062
- Churazov, E., Tremaine, S., Forman, W., et al. 2010, *MNRAS*, 404, 1165
- Colafrancesco, S., & Blasi, P. 1998, *Aph*, 9, 227
- Comerford, J. M., & Natarajan, P. 2007, *MNRAS*, 379, 190
- Condon, J. J., Broderick, J. J., Seielstad, G. A., Douglas, K., & Gregory, P. C. 1994, *AJ*, 107, 1829
- Condon, J. J., Cotton, W. D., Greisen, E. W., et al. 1998, *AJ*, 115, 1693
- Costa, E., & Loyola, P. 1998, *A&AS*, 131, 259
- de Palma, F., Brandt, T. J., Johannesson, G., et al. for the *Fermi*-LAT Collaboration 2013, Proc. 2012 Fermi Symp., eConf Proceedings C121028 (Washington, DC: NASA)
- Dennison, B. 1980, *ApJL*, 239, L93
- Dolag, K., & Enßlin, T. A. 2000, *A&A*, 362, 151
- Donnert, J., Dolag, K., Brunetti, G., et al. 2010a, *MNRAS*, 401, 47
- Donnert, J., Dolag, K., Brunetti, G., et al. 2013, *MNRAS*, 429, 3564
- Donnert, J., Dolag, K., Cassano, R., et al. 2010b, *MNRAS*, 407, 1565
- Dugger, L., Jeltama, T., & Profumo, S. 2010, *JCAP*, 12, 015
- Dutson, K. L., White, R. J., Edge, A. C., et al. 2013, *MNRAS*, 429, 2069
- Edmon, P. P., Kang, H., Jones, T. W., et al. 2011, *MNRAS*, 414, 3521
- Ellison, D. C., & Eichler, D. 1984, *ApJ*, 286, 691
- Enßlin, T., Pfrommer, C., Miniati, F., et al. 2011, *A&A*, 527, A99
- Enßlin, T. A., Biermann, P. L., Kronberg, P. P., et al. 1997, *ApJ*, 477, 560
- Enßlin, T. A., Pfrommer, C., Springel, V., et al. 2007, *A&A*, 473, 41
- Feretti, L., Giovannini, G., Govoni, F., et al. 2012, *A&ARv*, 20, 54
- Ferrari, C., Govoni, F., Schindler, S., et al. 2008, *SSRv*, 134, 93
- Fey, A. L., Ma, C., Arias, E. F., et al. 2004, *AJ*, 127, 3587
- Fouqué, P., Solanes, J. M., Sanchis, T., et al. 2001, *A&A*, 375, 770
- Fujita, Y., & Ohira, Y. 2012, *ApJ*, 746, 53
- Gavazzi, G., & Jaffe, W. 1982, in IAU Symp. 97, Extragalactic Radio Sources, ed. D. S. Heeschen & C. M. Wade (Cambridge: Cambridge Univ. Press), 89
- Gavazzi, G., & Jaffe, W. 1987, *A&A*, 186, L1
- Guo, F., & Oh, S. P. 2008, *MNRAS*, 384, 251
- Han, J., Frenk, C. S., Eke, V. R., et al. 2012, *MNRAS*, 427, 1651
- Helder, E. A., Vink, J., Bassa, C. G., et al. 2009, *Sci*, 325, 719
- Huang, X., Vertongen, G., & Weniger, C. 2012, *JCAP*, 01, 042
- Hudson, D. S., Mittal, R., Reiprich, T. H., et al. 2010, *A&A*, 513, A37
- Hudson, D. S., Reiprich, T. H., Clarke, T. E., et al. 2006, *A&A*, 453, 433
- James, F., & Roos, M. 1975, *CoPhC*, 10, 343
- Jeltama, T. E., & Profumo, S. 2011, *ApJ*, 728, 53
- Jones, T. W., & Kang, H. 2005, *Aph*, 24, 75
- Kang, H., & Jones, T. W. 1995, *ApJ*, 447, 944
- Kang, H., & Ryu, D. 2011, *ApJ*, 734, 18
- Kang, H., & Ryu, D. 2013, *ApJ*, 764, 95
- Kempner, J. C., Blanton, E. L., Clarke, T. E., et al. 2004, in Proc. The Riddle of Cooling Flows in Galaxies and Clusters of Galaxies, ed. T. Reiprich, J. Kempner, & N. Soker (Charlottesville, VA: Univ. Virginia), 335
- Keshet, U. 2010, arXiv:1011.0729
- Keshet, U., & Loeb, A. 2010, *ApJ*, 722, 737
- Kiuchi, R., Mori, M., Bicknell, G. V., et al. 2009, *ApJ*, 704, 240
- Kushnir, D., Katz, B., & Waxman, E. 2009, *JCAP*, 09, 024
- Kushnir, D., & Waxman, E. 2009, *JCAP*, 08, 002
- Lande, J., Ackermann, M., Allafort, A., et al. 2012, *ApJ*, 756, 5
- Loewenstein, M., Zweibel, E. G., & Begelman, M. C. 1991, *ApJ*, 377, 392
- Miniati, F. 2003, *MNRAS*, 342, 1009
- Miniati, F., Jones, T. W., Kang, H., et al. 2001a, *ApJ*, 562, 233
- Miniati, F., Ryu, D., Kang, H., et al. 2001b, *ApJ*, 559, 59
- Morlino, G., & Caprioli, D. 2012, *A&A*, 538, A81
- Neronov, A., Semikoz, D., & Vovk, I. 2010, *A&A*, 519, L6
- Neyman, J., & Pearson, E. S. 1928, *Biometrika*, 20, 175A
- Nolan, P. L., Abdo, A. A., Ackermann, M., et al. 2012, *ApJS*, 199, 31
- Owen, F. N., O'Dea, C. P., Inoue, M., et al. 1985, *ApJL*, 294, L85
- Perkins, J. S., Badran, H. M., Blaylock, G., et al. 2006, *ApJ*, 644, 148
- Petrosian, V. 2001, *ApJ*, 557, 560
- Pfrommer, C. 2008, *MNRAS*, 385, 1242
- Pfrommer, C. 2013, *ApJ*, 779, 10
- Pfrommer, C., & Dursi, L. J. 2010, *NatPh*, 6, 520
- Pfrommer, C., & Enßlin, T. A. 2003, *A&A*, 407, L73
- Pfrommer, C., & Enßlin, T. A. 2004a, *A&A*, 413, 17
- Pfrommer, C., & Enßlin, T. A. 2004b, *MNRAS*, 352, 76
- Pfrommer, C., Enßlin, T. A., & Springel, V. 2008, *MNRAS*, 385, 1211
- Pfrommer, C., Springel, V., Enßlin, T. A., et al. 2006, *MNRAS*, 367, 113
- Pinzke, A., Oh, S. P., & Pfrommer, C. 2013, *MNRAS*, 435, 1061
- Pinzke, A., & Pfrommer, C. 2010, *MNRAS*, 409, 449
- Pinzke, A., Pfrommer, C., & Bergström, L. 2011, *PhRvD*, 84, 123509
- Reimer, O., Pohl, M., Sreekumar, P., et al. 2003, *ApJ*, 588, 155
- Reiprich, T. H., & Böhringer, H. 2002, *ApJ*, 567, 716
- Rolke, W. A., López, A. M., & Conrad, J. 2005, *NIMPA*, 551, 493
- Ruszkowski, M., Lee, D., Brügggen, M., et al. 2011, *ApJ*, 740, 81
- Ryu, D., Kang, H., Hallman, E., et al. 2003, *ApJ*, 593, 599
- Schlickeiser, R. 2002, *Cosmic Ray Astrophysics* (Berlin: Springer)
- Schlickeiser, R., Sievers, A., & Thiemann, H. 1987, *A&A*, 182, 21
- Sivanandam, S., Zabudoff, A. I., Zaritsky, D., et al. 2009, *ApJ*, 691, 1787
- Skillman, S. W., O'Shea, B. W., Hallman, E. J., et al. 2008, *ApJ*, 689, 1063
- Spearman, C. 1904, *Am. J. Psychol.*, 15, 72
- Sreekumar, P., Bertsch, D. L., Dingus, B. L., et al. 1994, *ApJ*, 426, 105
- Storm, E. M., Jeltama, T. E., & Profumo, S. 2012, *ApJ*, 755, 117
- Strong, A. W., & Bignami, G. F. 1983, *ApJ*, 274, 549
- Su, M., Slatyer, T. R., & Finkbeiner, D. P. 2010, *ApJ*, 724, 1044
- Vazza, F., Brunetti, G., & Gheller, C. 2009, *MNRAS*, 395, 1333
- Vazza, F., Dolag, K., Ryu, D., et al. 2011, *MNRAS*, 418, 960
- Vestrand, W. T. 1982, *AJ*, 87, 1266
- Voit, G. M. 2005, *RvMP*, 77, 207
- Völk, H. J., Aharonian, F. A., & Breitschwerdt, D. 1996, *SSR*, 75, 279
- Wiener, J., Oh, S. P., & Guo, F. 2013, *MNRAS*, 434, 2209
- Zandanel, F., & Ando, S. 2013, arXiv:1312.1493
- Zimmer, S. J., Conrad, J. for the *Fermi*-LAT Collaboration, & Pinzke, A. 2011, in Proc. 2011 Fermi Symp., eConf Proceedings C110509 (Washington, DC: NASA), arXiv:1110.6863